

Exotic swarming dynamics of high-dimensional swarmalators

Akash Yadav^{1†}, Krishnanand J^{1†}, V.K. Chandrasekar²,
Wei Zou^{3,4}, Jürgen Kurths^{5,6}, D.V. Senthilkumar^{1*}

^{1*}School of Physics, Indian Institute of Science Education and Research
Thiruvananthapuram, Thiruvananthapuram, 695551, Kerala, India.

²Department of Physics, Center for Nonlinear Science and Engineering,
School of Electrical and Electronics Engineering, SASTRA Deemed
University, Thanjavur, 613401, Tamil Nadu, India.

³School of Mathematical Sciences, South China Normal University,
Guangzhou 510631, China.

⁴Research Institute of Intelligent Complex Systems, Fudan University,
Shanghai, 200433, China.

⁵Potsdam Institute for Climate Impact Research, Telegraphenberg
Potsdam , D-14415, Germany.

⁶Institute of Physics, Humboldt University Berlin, Berlin, D-12489,
Germany.

*Corresponding author(s). E-mail(s): skumar@iisertvm.ac.in;

Contributing authors: akashyadav23@iisertvm.ac.in;

krishnanandj2000@gmail.com; chandru25nld@gmail.com;

weizou83@gmail.com; kurths@pik-potsdam.de;

[†]These authors contributed equally to this work.

Abstract

Swarmalators are oscillators that can swarm as well as sync via a dynamic balance between their spatial proximity and phase similarity. We present a generalized D-dimensional swarmalator model, which is more realistic and versatile, that captures self-organizing behaviors of a plethora of real-world collectives. This allows for modeling complicated processes such as flocking, schooling of fish, cell sorting during embryonic development, residential segregation, and opinion dynamics in social groups. We demonstrate its versatility by capturing the manoeuvres of

school of fish and traveling waves of gene expression, both qualitatively and quantitatively, embryonic cell sorting, microrobot collectives and various life stages of slime mold by a suitable extension of the original model to incorporate appropriate features besides a gallery of its intrinsic self-organizations for various interactions. We expect this high-dimensional model to be potentially useful in describing swarming systems in a wide range of disciplines including physics of active matter, developmental biology, sociology, and engineering.

Keywords: Swarmalators, Complex Systems, Synchronization, Self-Organization

Introduction

Complex systems science aims at unravelling the underlying dynamical processes that are responsible for a plethora of self-organizing collective behaviors in various branches of science and technology including systems biology [1, 2], climate science [3, 4], complex networks [5, 6], ecology [7] and social studies [8, 9] in an effort towards the effective utilization of the natural resources, and their sustainability. A recent strongly emerging interest in complex systems science, which is gaining momentum, are studies on the swarming dynamics [10–17]. Swarmalators represent a class of systems which are able to self-aggregate spatially (swarm) and simultaneously adjust their internal rhythms (synchronize) through a delicate balance between their spatial proximity and phase similarity, representing the latter. Pioneering contributions were recently made by Igoshin et al. and Tanaka et al. in modeling the dynamics of chemotactic oscillators [18–20] and by Levis et al. in describing the dynamics of revolving agents [21, 22].

Recent surge in the studies on the swarmalators displayed a zoo of collective dynamical states mimicking the self-organizing dynamics of natural [23, 24] and technological [25–27] collectives ranging from spermatozoa [23] to drones and robots [28–30]. A recent study by O’Keeffe et al. [10] elucidated that static phase wave (SPW) is qualitatively similar to the ‘asters’ formed by the ferromagnetic colloids [31], whereas the active phase wave (APW) has the characteristic features of ‘vortex arrays’ formed by the populations of spermatozoa [23]. Generalization of the swarmalator model in [10] by including non-identical frequencies, chirality and local coupling, unveiled several new spatiotemporal regimes including interacting phase waves, vortices, and beating clusters [12]. It was also shown that many of these self-organizing patterns qualitatively resemble those exhibited by cellular self-organization [32, 33], flocking patterns of Quinke rollers [26, 34], and the various life stage of slime mold [35]. An attempt for an analytical description of the synchronized state and the existence condition for a few of the states using a basic model was presented recently [16]. Other extensions by including Gaussian function for short-range repulsive interaction [13], delayed interactions [15], and pinning [17] have also been made.

However, immediate applications of the observed swarming dynamics remain elusive despite the majority of them qualitatively resemble the emerging patterns of a

wide variety of real-world systems. Nevertheless, a direct comparison of several measurable observables from the minimalistic swarmalator model to that of experimental data elucidate that real-world applications of swarmalator models are imminent. One of the prospective applications of a reconfigurable swarmalator dynamics is their locomotive utility [10]. For instance, the collective metachronal waves known to facilitate biological transport [36, 37] of the populations of cilia are similar to APW and splintered phase wave (SPPW). Particularly, reconfigurable microrobot swarms, a perfect real-world example of swarmalators, can be used for biomedical applications including targeted drug delivery [29, 30, 38].

Given the tremendous potential real-world applications of swarmalators, the model employed in the aforementioned studies invariably comprises of evolution equations for two-dimensional spatial variables and one-dimensional Kuramoto model [39] governing the phase dynamics. However, most of these studies generalized their results to three-dimensional spatial variables, where the phase evolves on a unit circle in accordance with the spatial proximity but lacks the orientational degree of freedom. But this is a key component of almost all real-world swarmalators such as spin orientation in ferromagnetic collides [40], velocity vector of birds flock [41, 42], fish schools, and swarm of drones. The orientation degree of freedom is an intrinsic feature of all systems described by spherical polar coordinates, in which the orientation vector is specified by both polar angle θ and azimuthal angle ϕ . The internal state of such systems is inevitably described by the orientation vector represented in terms of θ and ϕ in three-dimensions (3D), which is missing in the existing studies on swarmalators.

To treat this important point, we introduce here a D-dimensional swarmalator model governed by D-dimensional spatial and orientation vectors, in general, for predictive fidelity of the self-organizing behaviors of real-world swarmalators, where the alignment of their orientation vectors represents their intrinsic dynamics. For more sensible visualization and interpretation of results, we restrict our simulations to 3D space and 3D phase variables. We show that in view of the inseparable dynamics of θ and ϕ affecting the spatial proximity and vice versa in 3D, our model indeed facilitates a repertoire of exotic self-organizing behaviors (see Table S1) that are specific to our model in addition to those states observed by the aforementioned studies with similar settings.

Results

The Model

The proposed D-dimensional swarmalator model is represented by

$$\dot{\mathbf{x}}_i = \mathbf{v}_i + \frac{1}{N-1} \sum_{j=1}^N \left[\{1 + J(\boldsymbol{\sigma}_i \cdot \boldsymbol{\sigma}_j)\} \frac{\mathbf{x}_j - \mathbf{x}_i}{|\mathbf{x}_j - \mathbf{x}_i|^\alpha} - \frac{\mathbf{x}_j - \mathbf{x}_i}{|\mathbf{x}_j - \mathbf{x}_i|^\beta} \right] + \boldsymbol{\xi}_i^x(t), \quad (1a)$$

$$\dot{\boldsymbol{\sigma}}_i = \mathbf{W}_i \boldsymbol{\sigma}_i + \sum_{j=1}^N K_{ij} \left[\frac{\boldsymbol{\sigma}_j - (\boldsymbol{\sigma}_j \cdot \boldsymbol{\sigma}_i) \boldsymbol{\sigma}_i}{|\mathbf{x}_j - \mathbf{x}_i|^\gamma} \right] + \boldsymbol{\xi}_i^\sigma(t), \quad (1b)$$

where $i = 1, 2, 3, \dots, N$ is the number of swarmalators, \mathbf{x}_i is the D -dimensional position vector of the i^{th} swarmalator, $\boldsymbol{\sigma}_i$ is its orientation vector on the D -dimensional unit hyper-sphere characterizing the intrinsic dynamics of the swarms, and \mathbf{v}_i is its self-propulsion velocity. Note that the evolution equation for $\boldsymbol{\sigma}_i$ in the absence of the distant dependent kernel is the D -dimensional Kuramoto model [42, 43] (see supplementary text S1 for its derivation). In the context of flocking and swarming models $\boldsymbol{\sigma}_i$ can be interpreted as the unit vector along the velocity vector of the i^{th} swarmalator [42], while in the context of social interactions, the alignment of opinion dynamics could, in general, be multidimensional [42, 43].

The first and second terms in Eq. (1a) correspond to the spatial attraction and repulsion. Spatial attraction between the swarmalators depends on the degree of orientation and the parameter J . The repulsive interaction is essential to maintain the minimum separation between agents. The nature of the distance-dependent spatial interactions can be tuned with the exponents α , β , and γ . The distant-dependent kernels in Eq. (1a) act like a Van der Waals interaction for $\beta > \alpha$ that ensures the long-range attraction and short-range repulsion. $\boldsymbol{\omega}_i$ is the anti-symmetric angular velocity $D \times D$ matrix of the i^{th} swarmalator, which can be represented in 3D as

$$\mathbf{W}_i = \begin{pmatrix} 0 & -\omega_{i,3} & \omega_{i,2} \\ \omega_{i,3} & 0 & -\omega_{i,1} \\ -\omega_{i,2} & \omega_{i,1} & 0 \end{pmatrix}, \quad (2)$$

where $\omega_{i,1}, \omega_{i,2}$ and $\omega_{i,3}$ represents the components of the angular velocity. The coupling strength K_{ij} is given as

$$K_{ij} = \begin{cases} \varepsilon_a/N_i & \text{for } |\mathbf{x}_j - \mathbf{x}_i| \leq R, \\ -\varepsilon_r/N_r & \text{for } |\mathbf{x}_j - \mathbf{x}_i| > R, \end{cases}$$

where ε_a is the attractive phase coupling strength, ε_r is the repulsive phase coupling strength, R is the vision radius, N_i is the number of swarmalators inside the vision sphere of the i^{th} swarmalator excluding it (Refer to the supplementary text S1 and fig. S1 for derivation of Eq. (1b)). $\boldsymbol{\xi}_i^{\mathbf{x}}(t)$ and $\boldsymbol{\xi}_i^{\boldsymbol{\sigma}}(t)$ are the Gaussian white noise with zero mean and strengths D_{x_k} and D_{σ_k} characterized by $\langle \boldsymbol{\xi}_i^{x_k}(t) | \boldsymbol{\xi}_i^{x_k}(t') \rangle = 2D_{x_k} \delta(t-t')$ and $\langle \boldsymbol{\xi}_i^{\sigma_k}(t) | \boldsymbol{\xi}_i^{\sigma_k}(t') \rangle = 2D_{\sigma_k} \delta(t-t')$, respectively, where $k = 1, 2, 3, \dots, D$. Note that $\boldsymbol{\sigma}_i$ has to be normalized at each time step to ensure it to be unit vector because of $\boldsymbol{\xi}_i^{\sigma_k}(t)$. Swarmalators in most real-world swarms only exchange interactions with its N_i -nearest neighbors that are within their sphere of influence resulting in the notion of vision radius. Swarmalators within the vision sphere tend to align their internal state, whereas the others $N_r = N - N_i - 1$ have the natural tendency to repel each other.

We discuss the following more important situations, while others are presented in the supplementary material. Refer to the methods section for details on simulation and parameters.

Competitive interaction

First we intend to exclusively unfold the influence of the competitive attractive and repulsive interactions among the orientation vectors on the intriguing self-organizing dynamics and therefore we fix $\varepsilon_a = \varepsilon_r = 0.5$. Some of the fascinating self-organized convergent multistable symphonies by the swarmalator collectives are depicted and demarcated in Fig. 1. Swarmalators with the angle of inclination $\rho_{ij} \in (\pi/2, \pi)$ are strongly attracted for $J < 0$ and hence the collectives display a static async (SA) for small R , as the majority of the swarmalators lie outside R with the tendency to repel each other. Swarmalators with $\rho_{ij} \in (0, \pi/2]$ are attracted strongly for $J > 0$ and exhibit SA for small R and J (fig. S10, text S4). Nevertheless, swarmalators with nearby σ are strongly attracted above appreciable J , even for small R , to self-organize to display a phase wave, which is active (APW) due to the competitive repulsion among the orientation vectors and weak spatial attraction as the majority of them lie outside R .

N_i increases progressively proportional to R resulting in the manifestation of multi-clusters (MC) from APW as R is increased, which eventually merges together to manifest as a single static synchronized (SS) cluster above a large R . The sufficient condition for synchronization can be obtained as $R > 1/\sqrt{1-J}$. Refer to the supplementary text S5 for the detailed derivation. Refer Table S1 for the description of the acronyms for observed states.

Now, each cluster in MC becomes sparse as J is decreased in the intermediate range of R , owing to a low degree of spatial attraction, and eventually the MC gather together with their preferred orientation to showcase spiky states (SP). Two such spiky states, namely twisted and flower states, are depicted in Fig. 1 (fig. S14A), where the orientation vectors are radially pointed outwards from the axis of symmetry in the flower state and vice versa in the twisted state. Note that the emergence of SP states are extended even for $J < 0$, though sparse than those for $J > 0$, as there lies a net positive spatial attraction for small $|J|$ and hence there is a meager local synchronization for the SP state to persist. Further decrease in J , in the same range of R , facilitates an active core static phase wave (ACSPW) with a turbulent core and the outer shell as the SPW. A strong attraction among the N_r swarmalators for $J < 0$ manifests the asynchronous core, while the synchronized swarmalators within R are weakly attracted leading to the SPW. Now, the swarmalators in the core that fall within R tend to synchronize and eventually repel outside of R to get asynchronized, which are again attracted, both due to $J < 0$, reinforcing the effect resulting in the active core. An increase in R for $J > 0$ from SP increases N_i resulting in the synchronized core and the rest N_r swarmalators form a SPW shielding the core, such a coexisting of coherent and incoherent domains are known as chimera (CH). The coherent core increases with R and eventually CH manifests as SS for a large R . CH and SS transforms to a turning tube (TT) for $J < 0$, as the spatial attraction among the incoherent domain is stronger, which remains rolling with N_i like the active core in ACSPW.

Order parameters delineating the dynamical transitions as a function of R for three distinct J are depicted in fig. S6. It is important to emphasize that the observed self-organizing behaviors are robust against Gaussian noise (fig. S12). Emerging dynamical

behaviors for the attraction(repulsion) dominated competitive interaction are depicted in fig. S13(S15). Phase diagrams with $\omega_i = 0$, two, and distributed orthogonal angular frequencies are respectively presented in figs. A B, and C of figs. S13-S15. Refer to the supplementary text S6-S8 for discussions. The heat maps of the employed order parameters corresponding to figs. S13A-S15A are shown in fig. S16.

Extreme R and local attractive coupling

Swarmalator collectives exclusively display SS(SA) for $N_i = N - 1$ ($N_r = N - 1$) as all of them experience only attractive(repulsive) phase coupling. Nevertheless, the collectives exhibit alluring patterns for exclusive local attractive coupling among the orientation vectors as a function of R especially for $J < 0$ (see Fig. 2). Here, we uncover a transition from SA to SPW in contrast to the transition from SA to APW in the competitive interaction as a function of J in the low range of R as the influence of spatial proximity is absent on the swarmalators that lie outside R . SPW manifests as SS via MC as R is increased for $J > 0$. There is a transition from SA to SS via mixed synchronized state (MSS) as R is increased for $J < 0$. SS becomes more and more dense(sparse) for $J > 0$ ($J < 0$) (Figs. 2A to 2D) as the spatial attractive coupling strength increasingly becomes stronger(weaker) as J is increased (decreased). MC of similar sizes are formed for $R = 0.5$ with a weak spatial attraction within the clusters and a strong spatial attraction among the clusters resulting in the MSS. The size of some of the synchronized clusters increases with R that are spatially sparse (see Figs. 2F-2G). See fig. S17(S18) and text S9(S10) for the comparison with two, and distributed orthogonal angular frequencies for $\varepsilon_r = 0$ ($N_r = N - 1$).

Competitive interaction with quenched disorder

Next, we explore the effect of quenched disorder, $\mathbf{W}_i \sigma_i$, on the swarming dynamics due to the competitive interactions among the orientation vectors. We consider equally distributed orthogonal angular frequencies $\omega_1 = [1, 0, 0]$ and $\omega_2 = [0, 1, 0]$ for sustained precession of the orientation vectors. The swarmalators quench their precession (movie S8) leading to non-chiral collective states as in Figs. 1 and 2 for other choices of $\omega_{1,2}$.

Effectively, $\mathbf{W}_i \sigma_i$ in Eq. (1b) induces a dispersion among the orientation vectors that lead to distinct chiral states with precessing swarmalators (see Fig. 3). The influence of R and J are similar to those discussed in Fig. 2. For low values of R , disordered spin (DS) manifests as spinning spiky (SSP) states above a critical value of $J > 0$. From SSP, a synchronized spinning state (SSS) is formed via a multi-cluster bouncing spin (MCBS) state as R is increased. A pumping state (PS) mediates the transition from DS to SSS. The density of SSS decreases as $J \rightarrow -1$ as in Fig. 2. Precessing orientation vectors recursively results in their coherence and decoherence, which dynamically establishes dense and sparse synchronized clusters, respectively. The dense clusters repel each other, whereas the swarmalators in the sparse clusters that fall within their R are synchronized resulting in the reinforcement of MCBS for $J > 0$. A similar mechanism underlies the onset of PS for $J < 0$, where recursive coherence and decoherence result in sparse synchronous and dense asynchronous

collectives dynamically resulting in the PS.

Real-Worlds Systems

Now we show that our extended model (1) is indeed able to capture the following important real-world swarms.

Schooling of Fish

We display the defensive manoeuvre of a real school of fish by including self-propelling velocity and modifying the repulsive interaction among the orientation vectors to include the centripetal inclination of the fishes towards their center of mass to evade predation (see supplementary text S11 for model description). We have used the experimental data [44] to depict the snapshots of crystal and milling behavior [45, 46] of a school of fish in Figs. 4A and 4C. Self-organizing dynamics of our model very well mimic the observed crystal and milling behaviors as depicted in Figs. 4B and 4D, respectively. Some more rich behaviors of a school of fish can be found in fig. S19. Phase diagrams and heat maps of order parameters are depicted in figs. S20-S21. The synchronization S and the spatial vorticity Γ_x order parameters, defined in the supplementary text S11, for both the experimental and the simulation data (see movies S25 (simulation) and S26 (experiment) depicting the evolution of the dynamical states and the order parameters) are shown in Figs. 4E and 4F, respectively. The null value of $S(\Gamma_x)$ and unit value of $\Gamma_x(S)$ corroborates the milling(crystal) behavior for $t > 300(t > 700)$. The striking similarities of S and Γ_x for both the experimental and the model data establish the significance of our model in predicting excellently the dynamics of a school of fish both qualitatively and quantitatively.

Traveling waves of gene expression

Embryonic stem cells exhibit traveling phase wave, triggered by genetic oscillators, are suspected as the key to the puzzle of constant vertebrae segment numbers of mouse embryonic cells even when the embryonic size is reduced [47]. In vivo fluorescence image and kymograph of LuVeLu activity in mouse embryo are shown in Figs. 4G and 4H, respectively. Analogous patterns exhibited by the model (1) with the local spatial interaction are depicted in Figs. 4I and 4J, respectively. The normalized mean intensity of the fluorescence exhibiting traveling phase wave and the corresponding simulation results are presented in Figs. 4K and 4L, respectively. The supplementary movie S27 displays the traveling phase wave exhibited by the swarmalator collectives, which has striking resemblances with the in vivo real-time imaging of genetic oscillations found in the supplementary video 1 of Ref. [47]. These remarkable similarities elucidate that our generalized model provides valuable insights on the embryonic pattern formation.

Embryonic Cell Sorting

Embryonic cell sorting is a process, occurring during embryonic development, in which cells spontaneously sort and aggregate to form tissue patterns [48] based on their

cell type and adhesion properties. In vitro fluorescence image of initially dissociated embryonic cells in Fig. 5A [49] sort themselves and aggregate together to form tissue patterns as in Fig. 5C. Analogously, random distribution of three populations of swarmalators in Fig. 5B, see supplementary text S12 for model description, self-aggregate into organized populations (tissue layers) in accordance with their adhesive nature (see Fig. 5D). The supplementary movie S28 displays the aggregation of swarmalators mimicking cell sorting. More precise modeling is possible by incorporating further details, such as cell division, cell death and cell differentiation.

Microrobot Collectives

Several experimental studies illustrated the self-organizing collective states of microrobots, which has potential medical and environmental applications [50, 51]. The increasingly sparse static sync state (see Fig. 2 for $J < 0$) is depicted in Figs. 5F, 5J and 5N resembles the spatial patterns of the spinning magnetic micro-disks in Figs. 5E, 5I and 5M [50]. We strongly believe that the rich self-organizing patterns exhibited by the minimalistic swarmalator model (1) can enhance the utility of microrobots.

Aggregation in *Dicyostelium discoideum*

Dicyostelium discoideum is a cellular slime mold with unusual life cycle. The separately existing single-celled amoebae form multicellular structures in response to the environmental stress [52] (see Figs. 5G, 5K, and 5O). The aggregation of our swarmalator model (1) with local spatial interactions captures different life stages of the slime mold (see Figs. 5H, 5L and 5P, supplementary movie S29).

Discussion

We have proposed a D-dimensional swarmalator model and unveiled a rich variety of multistable collective behaviors, tabulated in the supplementary Table S1, in the phase diagrams. Most of which are only generated in our generalized model (1) and only some of them were also observed in models discussed in the literature. We have defined suitable order parameters to characterize and classify the distinct self-organized collective states. As pointed out, the SPW and APW qualitatively resemble with the ‘asters’ observed in magnetic colloids and ‘vortex arrays’ formed by populations of spermatozoa, respectively. Notably, spiky states have striking resemblance with the ‘skyrmions’ observed in magnetic materials [53], which is a potential candidate for future data-storage solutions and other spintronics devices. Other detected behaviors are also promising to be identified in several real-world systems. The qualitative resemblance will set a stage for a further deep theoretical investigation of the minimalistic swarmalator model with essential extensions.

We have provided the first evidences of strong potentials of our model. In particular, we have extended the original model to successfully capture the schooling behavior of fishes, traveling phase wave of genetic oscillator both qualitatively and quantitatively, embryonic cell sorting, microrobots and various life stages of slime mold. The insights on the underlying mechanisms of self-organization of cells can be useful in

synthetic engineering tissues and organs for clinical purposes [54–56]. We strongly believe that our model can be used to unfold the underlying mechanism behind self-organizing properties of micro- and nano-swimmers, self-propelling agents, microrobot collectives, etc. In particular, the transportation properties of microrobot collectives can be better controlled using our model for more precise drug delivery and other biomedical applications. Furthermore, strategic formation by drones and precise control of their collective functions using our model can be used for security purposes, rescue operations, explorations, etc. Specific interest could be studying reconfigurable microrobots for potential applications including understanding self-healing structures.

Methods

Numerical Simulations and Visualization

We have numerically solved Eq. (1) using the Runge Kutta 4th order integration scheme with a step size of 0.1. Initial conditions for the position vectors are randomly drawn from a 3D cube of length 2 with each side being uniformly distributed between $[-1, 1]$ and that for the orientation vectors are randomly drawn from the uniform distributions $\theta \in [0, \pi]$ and $\phi \in [0, 2\pi)$. We have fixed $\mathbf{v}_i = \boldsymbol{\omega}_i = D_{x_k} = D_{\sigma_k} = 0$, $\alpha = 1$, $\beta = 3$, $\gamma = 1$, $N = 100$, and distinct self-organizing behaviors are classified in the (J, R) parameter space in the range of $J \in [-1, 1]$ and $R \in [0, 2]$ throughout the manuscript unless otherwise specified.

Each swarmalator is represented by a cone (colored according to the heat map, fig. S1) with its apex pointing along the orientation vector. To test the robustness of the collective states observed in our high-dimensional swarmalator model, we have used zero mean white noise with varying noise strengths (D_{x_k}, D_{σ_k}) of 0.00, 0.01, 0.03. We have observed that the self-organized states are retained despite the presence of noise (fig. S12).

Order Parameters

We have used distinct order parameters to characterize and classify the distinct self-organizing collective behaviors (see Table S1). The synchronization order parameter quantifies the degree of coherence of the orientation vectors of the swarmalators, which can be defined as the norm of the average orientation of all the swarmalators, represented as

$$S = \frac{1}{N} \left| \sum_{j=1}^N \boldsymbol{\sigma}_j \right|, \quad (3)$$

where $\boldsymbol{\sigma}_j$ is the orientation vector of the j^{th} swarmalator. The synchronization order parameter S varies in the range $[0, 1]$. The asynchronized state will have $S = 0$ whereas the synchronized state is characterized by $S = 1$. The intermediate value of S between 0 and 1 quantify the degree of coherence among the orientation vectors.

The orientation parameter quantifies the degree of alignment of the orientation vector of the i^{th} swarmalator with respect to its position vector (fig. S2). The orientation parameter is used to distinguish distinct spiky states such as flower state, twisted

state and star state.

$$\Lambda = \frac{1}{N} \sum_{i=1}^N \frac{\mathbf{x}_i \cdot \boldsymbol{\sigma}_i}{|\mathbf{x}_i| |\boldsymbol{\sigma}_i|}, \quad (4)$$

where \mathbf{x}_i is the position vector of the i^{th} swarmalator. The orientation parameter Λ can vary in the range $[-1, 1]$. The star state (see Table S1), in which all swarmalators have orientations pointing radially outwards from the sphere would have $\Lambda = 1$. An inverted star state (in which all swarmalators would point radially inwards) would take a Λ value -1 . Intermediate values of Λ characterizes the degree of orientation of the swarmalators in spiky states such as flower state, and twisted state.

The collective states with a spherical cavity as their core such as in spiky states and active phase wave are characterized using the hollowness parameter defined as

$$H = \frac{\min \{|\mathbf{x}_i|\}}{\max \{|\mathbf{x}_i|\}} \quad i = 1, 2, \dots, N. \quad (5)$$

The hollowness parameter H can vary between 0 and 1. Solid spherical states such as static phase wave, synchronized states are characterized by $H = 0$. Intermediate values of H between 0 and 1 quantify the degree of spherical cavity forming the core of the collective states. Asymptotically active states are characterized using the kinetic energy parameter defined as

$$K = \frac{1}{N} \sum_{i=1}^N \dot{\mathbf{x}}_i^2. \quad (6)$$

The nonzero values of K indicate that the collective state is dynamic, whereas near zero values indicate that the collective state is static. The kinetic energy parameter is depicted as a function of time for the spinning cluster, active phase wave and static synchronized state in fig. S3.

We have used K-means clustering method to identify the number of clusters (N_c) using the spatial and orientation data. For implementation of this algorithm, ‘kmeans’ function from the scikit-learn python library is used. K-means algorithm segregates the swarmalators into K clusters by iteratively minimizing the clustering error(ξ).

$$\xi = \sum_{K'=1}^K \sum_{i=1}^{N_{K'}} \left| \mathbf{x}_i^{K'} - \boldsymbol{\mu}^{K'} \right|^2 \quad (7)$$

where $\boldsymbol{\mu}^{K'}$ is the center of K' cluster. The elbow point(K_{best}) gives the estimate for number of cluster. Refer to supplementary text S2 for more details about K-means clustering approach.

Declarations

- **Funding** : This project was supported by the DST-SERB-CRG Project under Grant No. CRG/2021/000816.

- **Conflict of interest/Competing interests:** Authors declare that they have no competing interests.
- **Consent for publication :** All authors declare consent for the publication of the preseted work as research article.
- **Availability of data and materials :** All of the data are available in the main text or the supplementary materials. The custom codes used for simualtion are avaiable upon request to the corresponding author.
- **Authors' contributions :**
 Conceptualization: DVS, VKC, WZ
 Methodology: DVS, AY, KJ, VKC, WZ, JK
 Investigation: DVS, AY, KJ, VKC, WZ, JK
 Visualization: AY, KJ
 Supervision: DVS, JK
 Writing - original draft: DVS, AY, KJ, VKC, WZ, JK

Supplementary information. This article has following accompanying supplementary information.

Supplementary Text
 Figures S1 to S21
 Table S1
 References (1-7)
 Movies S1 to S29

Acknowledgments. The work of V.K.C. is supported by DST-CRG Project under Grant No. CRG/2020/004353 and VKC wish to thank DST, New Delhi for computational facilities under the DST-FIST programme (SR/FST/PS- 1/2020/135) to the Department of Physics. DVS is supported by the DST-SERB-CRG Project under Grant No. CRG/2021/000816.

References

- [1] Ross, J., Arkin, A.P.: Complex systems: From chemistry to systems biology. Proceedings of the National Academy of Sciences **106**(16), 6433–6434 (2009) <https://doi.org/10.1073/pnas.0903406106>
<https://www.pnas.org/doi/pdf/10.1073/pnas.0903406106>
- [2] Muñoz, M.A.: Colloquium: Criticality and dynamical scaling in living systems. Rev. Mod. Phys. **90**, 031001 (2018) <https://doi.org/10.1103/RevModPhys.90.031001>
- [3] Fan, J., Meng, J., Ludescher, J., Chen, X., Ashkenazy, Y., Kurths, J., Havlin, S., Schellnhuber, H.J.: Statistical physics approaches to the complex earth system. Phys Rep **896**, 1–84 (2020)

- [4] Boers, N., Goswami, B., Rheinwalt, A., Bookhagen, B., Hoskins, B., Kurths, J.: Complex networks reveal global pattern of extreme-rainfall teleconnections. *Nature* **566**(7744), 373–377 (2019)
- [5] Pastor-Satorras, R., Castellano, C., Van Mieghem, P., Vespignani, A.: Epidemic processes in complex networks. *Rev. Mod. Phys.* **87**, 925–979 (2015) <https://doi.org/10.1103/RevModPhys.87.925>
- [6] Liu, Y.-Y., Slotine, J.-J., Barabási, A.-L.: Controllability of complex networks. *Nature* **473**(7346), 167–173 (2011) <https://doi.org/10.1038/nature10011>
- [7] Grimm, V., Revilla, E., Berger, U., Jeltsch, F., Mooij, W.M., Railsback, S.F., Thulke, H.-H., Weiner, J., Wiegand, T., DeAngelis, D.L.: Pattern-oriented modeling of agent-based complex systems: Lessons from ecology. *Science* **310**(5750), 987–991 (2005) <https://doi.org/10.1126/science.1116681>
- [8] Levin, S.A., Milner, H.V., Perrings, C.: The dynamics of political polarization. *Proceedings of the National Academy of Sciences* **118**(50), 2116950118 (2021) <https://doi.org/10.1073/pnas.2116950118> <https://www.pnas.org/doi/pdf/10.1073/pnas.2116950118>
- [9] Sekara, V., Stopczynski, A., Lehmann, S.: Fundamental structures of dynamic social networks. *Proceedings of the National Academy of Sciences* **113**(36), 9977–9982 (2016) <https://doi.org/10.1073/pnas.1602803113> <https://www.pnas.org/doi/pdf/10.1073/pnas.1602803113>
- [10] O' Keeffe, K.P., Hong, H., Strogatz, S.H.: Oscillators that sync and swarm. *Nature Communications* **8**(1), 1504 (2017) <https://doi.org/10.1038/s41467-017-01190-3>
- [11] Sar, G.K., Chowdhury, S.N., Perc, M., Ghosh, D.: Swarmalators under competitive time-varying phase interactions. *New Journal of Physics* **24**(4), 043004 (2022) <https://doi.org/10.1088/1367-2630/ac5da2>
- [12] Ceron, S., O' Keeffe, K., Petersen, K.: Diverse behaviors in non-uniform chiral and non-chiral swarmalators. *Nature Communications* **14**(1), 940 (2023)
- [13] Jiménez-Morales, F.: Oscillatory behavior in a system of swarmalators with a short-range repulsive interaction. *Phys. Rev. E* **101**, 062202 (2020) <https://doi.org/10.1103/PhysRevE.101.062202>
- [14] Japón, P., Jiménez-Morales, F., Casares, F.: Intercellular communication and the organization of simple multicellular animals. *Cells & Development* **169**, 203726 (2022) <https://doi.org/10.1016/j.cdev.2021.203726>
- [15] Blum, N., Li, A., O' Keeffe, K., Kogan, O.: Swarmalators with delayed interactions. *arXiv:2210.11417* (2022) <https://doi.org/10.48550/ARXIV.2210.11417>

- [16] Yoon, S., Keeffe, K.P.O., Mendes, J.F.F., Goltsev, A.V.: Sync and swarm: Solvable model of nonidentical swarmalators. *Physical Review Letters* **129**, 208002 (2022) <https://doi.org/10.1103/PHYSREVLETT.129.208002>
- [17] Sar, G.K., Ghosh, D., O' Keeffe, K.: Pinning in a system of swarmalators. *Phys. Rev. E* **107**, 024215 (2023) <https://doi.org/10.1103/PhysRevE.107.024215>
- [18] Igoshin, O.A., Mogilner, A., Welch, R.D., Kaiser, D., Oster, G.: Pattern formation and traveling waves in myxobacteria: Theory and modeling. *Proceedings of the National Academy of Sciences* **98**(26), 14913–14918 (2001) <https://doi.org/10.1073/pnas.221579598> <https://www.pnas.org/doi/pdf/10.1073/pnas.221579598>
- [19] Tanaka, D.: General chemotactic model of oscillators. *Physical Review Letters* **99**, 134103 (2007) <https://doi.org/10.1103/PHYSREVLETT.99.134103/FIGURES/1/MEDIUM>
- [20] Iwasa, M., Iida, K., Tanaka, D.: Various collective behavior in swarm oscillator model. *Physics Letters A* **376**(30), 2117–2121 (2012) <https://doi.org/10.1016/j.physleta.2012.05.025>
- [21] Levis, D., Liebchen, B.: Simultaneous phase separation and pattern formation in chiral active mixtures. *Phys. Rev. E* **100**, 012406 (2019) <https://doi.org/10.1103/PhysRevE.100.012406>
- [22] Levis, D., Pagonabarraga, I., Liebchen, B.: Activity induced synchronization: Mutual flocking and chiral self-sorting. *Phys. Rev. Res.* **1**, 023026 (2019) <https://doi.org/10.1103/PhysRevResearch.1.023026>
- [23] Riedel, I.H., Kruse, K., Howard, J.: A self-organized vortex array of hydrodynamically entrained sperm cells. *Science* **309**(5732), 300–303 (2005) <https://doi.org/10.1126/science.1110329> <https://www.science.org/doi/pdf/10.1126/science.1110329>
- [24] Swiecicki, J.-M., Sliusarenko, O., Weibel, D.B.: From swimming to swarming: *Escherichia coli* cell motility in two-dimensions. *Integrative Biology* **5**(12), 1490–1494 (2013) <https://doi.org/10.1039/c3ib40130h> <https://academic.oup.com/ib/article-pdf/5/12/1490/27301612/c3ib40130h.pdf>
- [25] Sumino, Y., Nagai, K.H., Shitaka, Y., Tanaka, D., Yoshikawa, K., Chaté, H., Oiwa, K.: Large-scale vortex lattice emerging from collectively moving microtubules. *Nature* **483**(7390), 448–452 (2012)
- [26] Han, K., Kokot, G., Tovkach, O., Glatz, A., Aranson, I.S., Snezhko, A.: Emergence of self-organized multivortex states in flocks of active rollers. *Proceedings of the National Academy of Sciences* **117**(18), 9706–9711 (2020) <https://doi.org/10.1073/pnas.2000061117> <https://www.pnas.org/doi/pdf/10.1073/pnas.2000061117>

- [27] Yan, J., Bae, S.C., Granick, S.: Rotating crystals of magnetic janus colloids. *Soft Matter* **11**, 147–153 (2015) <https://doi.org/10.1039/C4SM01962H>
- [28] Barciś, A., Bettstetter, C.: Sandsbots: Robots that sync and swarm. *IEEE Access* **8**, 218752–218764 (2020) <https://doi.org/10.1109/ACCESS.2020.3041393>
- [29] Miskin, M.Z., Cortese, A.J., Dorsey, K., Esposito, E.P., Reynolds, M.F., Liu, Q., Cao, M., Muller, D.A., McEuen, P.L., Cohen, I.: Electronically integrated, mass-manufactured, microscopic robots. *Nature* **584**(7822), 557–561 (2020) <https://doi.org/10.1038/s41586-020-2626-9>
- [30] Talamali, M.S., Saha, A., Marshall, J.A.R., Reina, A.: When less is more: Robot swarms adapt better to changes with constrained communication. *Science Robotics* **6**(56), 1416 (2021) <https://doi.org/10.1126/scirobotics.abf1416> <https://www.science.org/doi/pdf/10.1126/scirobotics.abf1416>
- [31] Snezhko, A., Aranson, I.S.: Magnetic manipulation of self-assembled colloidal asters. *Nature Materials* **10**(9), 698–703 (2011) <https://doi.org/10.1038/nmat3083>
- [32] Tsiairis, C., Aulehla, A.: Self-organization of embryonic genetic oscillators into spatiotemporal wave patterns. *Cell* **164**(4), 656–667 (2016) <https://doi.org/10.1016/j.cell.2016.01.028>
- [33] Uriu, K., Morelli, L.G.: Determining the impact of cell mixing on signaling during development. *Development, Growth & Differentiation* **59**(5), 351–368 (2017) <https://doi.org/10.1111/dgd.12366> <https://onlinelibrary.wiley.com/doi/pdf/10.1111/dgd.12366>
- [34] Zhang, B., Sokolov, A., Snezhko, A.: Reconfigurable emergent patterns in active chiral fluids. *Nature Communications* **11** (2020)
- [35] Song, L., Nadkarni, S.M., Bödeker, H.U., Beta, C., Bae, A., Franck, C., Rappel, W.-J., Loomis, W.F., Bodenschatz, E.: Dictyostelium discoideum chemotaxis: Threshold for directed motion. *European Journal of Cell Biology* **85**(9), 981–989 (2006) <https://doi.org/10.1016/j.ejcb.2006.01.012>
- [36] Wong, L.B., Miller, I.F., Yeates, D.B.: Nature of the mammalian ciliary metachronal wave. *Journal of Applied Physiology* **75**(1), 458–467 (1993) <https://doi.org/10.1152/jap.1993.75.1.458> <https://doi.org/10.1152/jap.1993.75.1.458>. PMID: 8376297
- [37] Elgeti, J., Gompper, G.: Emergence of metachronal waves in cilia arrays. *Proceedings of the National Academy of Sciences* **110**(12), 4470–4475 (2013) <https://doi.org/10.1073/pnas.1218869110> <https://www.pnas.org/doi/pdf/10.1073/pnas.1218869110>

- [38] Gardi, G., Ceron, S., Wang, W., Petersen, K., Sitti, M.: Microrobot collectives with reconfigurable morphologies, behaviors, and functions. *Nature communications* **13**(1), 2239 (2022)
- [39] Acebrón, J.A., Bonilla, L.L., Pérez Vicente, C.J., Ritort, F., Spigler, R.: The kuramoto model: A simple paradigm for synchronization phenomena. *Rev. Mod. Phys.* **77**, 137–185 (2005) <https://doi.org/10.1103/RevModPhys.77.137>
- [40] Kaiser, A., Snezhko, A., Aranson, I.S.: Flocking ferromagnetic colloids. *Science Advances* **3**(2), 1601469 (2017) <https://doi.org/10.1126/sciadv.1601469> <https://www.science.org/doi/pdf/10.1126/sciadv.1601469>
- [41] Vicsek, T., Czirók, A., Ben-Jacob, E., Cohen, I., Shochet, O.: Novel type of phase transition in a system of self-driven particles. *Phys. Rev. Lett.* **75**, 1226–1229 (1995) <https://doi.org/10.1103/PhysRevLett.75.1226>
- [42] Chandra, S., Girvan, M., Ott, E.: Continuous versus discontinuous transitions in the d -dimensional generalized kuramoto model: Odd d is different. *Phys. Rev. X* **9**, 011002 (2019) <https://doi.org/10.1103/PhysRevX.9.011002>
- [43] Kovalenko, K., Dai, X., Alfaro-Bittner, K., Raigorodskii, A.M., Perc, M., Boccaletti, S.: Contrarians synchronize beyond the limit of pairwise interactions. *Phys. Rev. Lett.* **127**, 258301 (2021) <https://doi.org/10.1103/PhysRevLett.127.258301>
- [44] Katz, Y., Tunstrøm, K., Ioannou, C.C., Huepe, C., Couzin, I.D.: Fish schooling data subset. Fish Schooling Data Subset (Version 1). Oregon State University. url: <https://ir.library.oregonstate.edu/concern/datasets/zk51vq07c> (2021) <https://doi.org/10.7267/zk51vq07c>
- [45] Strömbom, D., Siljestam, M., Park, J., Sumpter, D.J.T.: The shape and dynamics of local attraction. *European Physical Journal: Special Topics* **224**, 3311–3323 (2015) <https://doi.org/10.1140/EPJST/E2015-50082-8>
- [46] Lopez, U., Gautrais, J., Couzin, I.D., Theraulaz, G.: From behavioural analyses to models of collective motion in fish schools. *Interface Focus* **2**, 693–707 (2012) <https://doi.org/10.1098/RFSFS.2012.0033>
- [47] Lauschke, V.M., Tsiairis, C.D., François, P., Aulehla, A.: Scaling of embryonic patterning based on phase-gradient encoding. *Nature* **493**(7430), 101–105 (2013) <https://doi.org/10.1038/nature11804>
- [48] Schötz, E., Burdine, R.D., Jülicher, F., Steinberg, M.S., Heisenberg, C., Foty, R.A.: Quantitative differences in tissue surface tension influence zebrafish germ layer positioning. *HFSP Journal* **2**(1), 42–56 (2008) <https://doi.org/10.2976/1.2834817> <https://doi.org/10.2976/1.2834817>. PMID: 19404452

- [49] Foty, R.A., Steinberg, M.S.: The differential adhesion hypothesis: a direct evaluation. *Developmental Biology* **278**(1), 255–263 (2005) <https://doi.org/10.1016/j.ydbio.2004.11.012>
- [50] Wang, W., Gardi, G., Margaretti, P., Kishore, V., Koens, L., Son, D., Gilbert, H., Wu, Z., Harwani, P., Lauga, E., Holm, C., Sitti, M.: Order and information in the patterns of spinning magnetic micro-disks at the air-water interface. *Science Advances* **8**(2), 0685 (2022) <https://doi.org/10.1126/sciadv.abk0685>
- [51] Gardi, G., Ceron, S., Wang, W., Petersen, K., Sitti, M.: Microrobot collectives with reconfigurable morphologies, behaviors, and functions. *Nature Communications* **13**(1), 2239 (2022) <https://doi.org/10.1038/s41467-022-29882-5>
- [52] Gregor, T., Fujimoto, K., Masaki, N., Sawai, S.: The onset of collective behavior in social amoebae. *Science* **328**(5981), 1021–1025 (2010)
- [53] Göbel, B., Mertig, I., Tretiakov, O.A.: Beyond skyrmions: Review and perspectives of alternative magnetic quasiparticles. *Physics Reports* **895**, 1–28 (2021) <https://doi.org/10.1016/j.physrep.2020.10.001>
- [54] Davies, J.A.: Synthetic morphology: prospects for engineered, self-constructing anatomies. *Journal of Anatomy* **212**(6), 707–719 (2008) <https://doi.org/10.1111/j.1469-7580.2008.00896.x> <https://onlinelibrary.wiley.com/doi/pdf/10.1111/j.1469-7580.2008.00896.x>
- [55] Toda, S., Blauch, L.R., Tang, S.K.Y., Morsut, L., Lim, W.A.: Programming self-organizing multicellular structures with synthetic cell-cell signaling. *Science* **361**(6398), 156–162 (2018) <https://doi.org/10.1126/science.aat0271> <https://www.science.org/doi/pdf/10.1126/science.aat0271>
- [56] Shafiee, A., Ghadiri, E., Langer, R.: Fabricating human tissues: How physics can help. *Physics Today* **75**(12), 38–43 (2022) <https://doi.org/10.1063/PT.3.5138> <https://doi.org/10.1063/PT.3.5138>

Figures

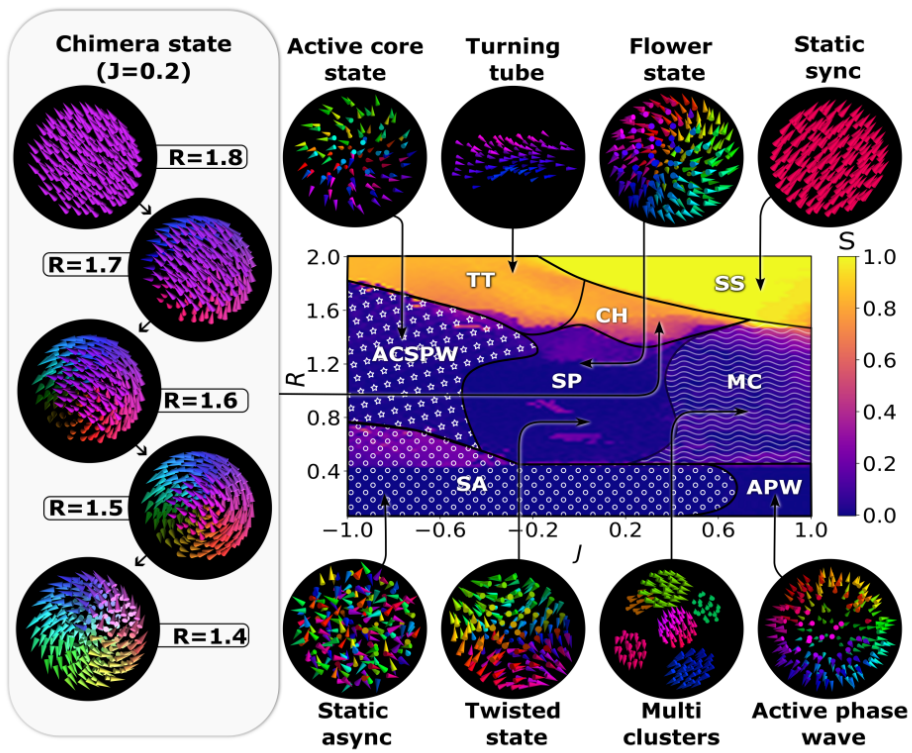


Fig. 1 Synchronization order parameter S is depicted as the heat map for $\varepsilon_a = \varepsilon_r = 0.5$ in the (J, R) space. Refer to the text for details.

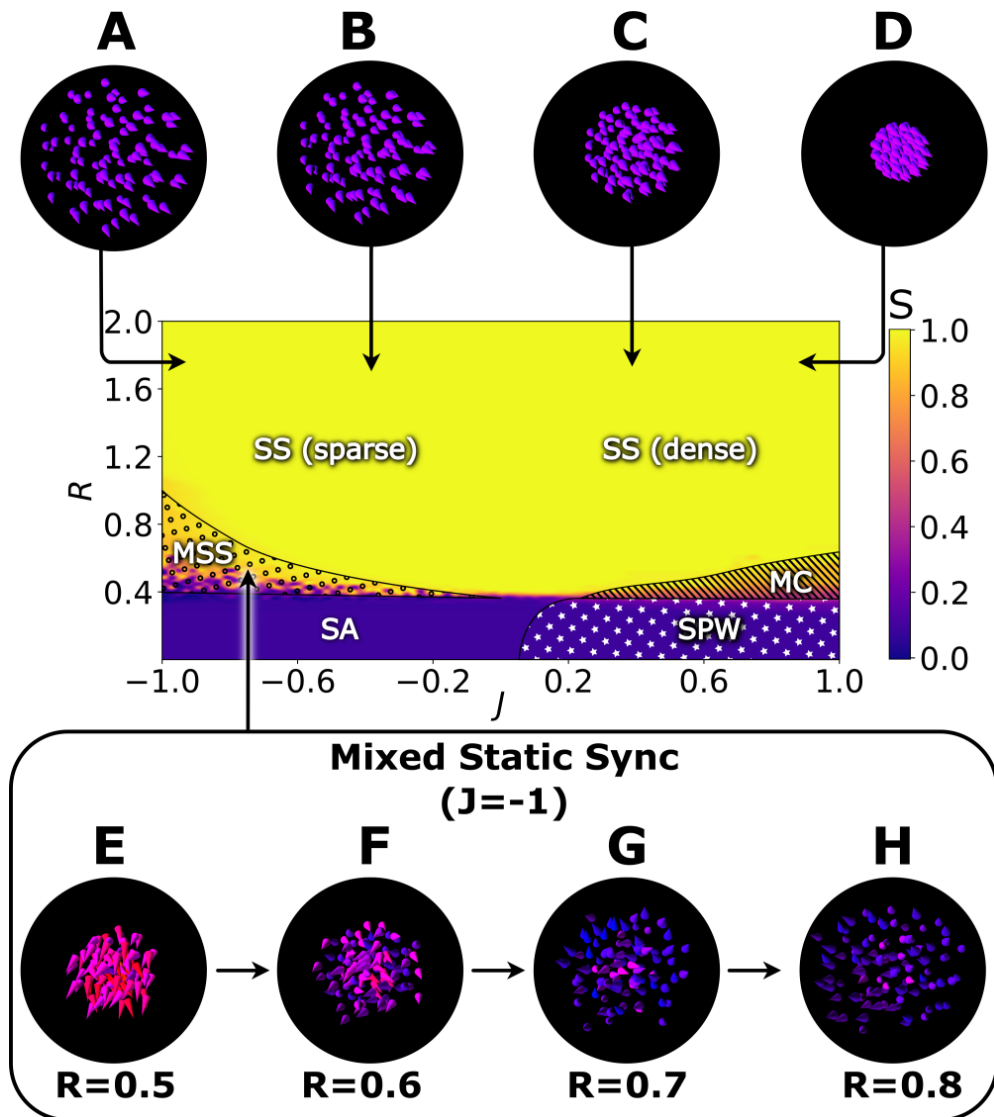


Fig. 2 Synchronization order parameter S is depicted as the heat map for $\varepsilon_a = 0.5$, and $\varepsilon_r = 0$ in the (J, R) space. Refer to the text for details.

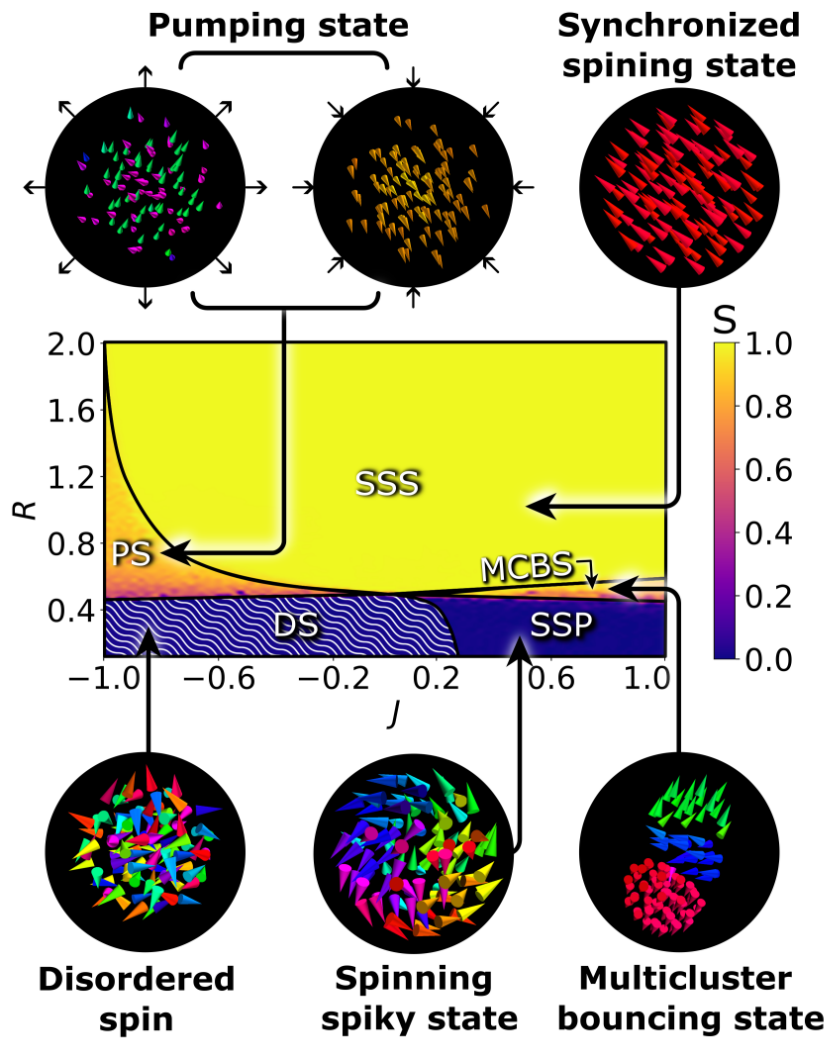


Fig. 3 Swarmalators with orthogonal angular frequencies. Simulations are performed for $N = 100, \varepsilon_a = 0.9, \varepsilon_r = 0.1$. The pumping state is a dynamic state in which swarmalators compress and expand in a rhythmic pattern reminiscent of the beating of the heart.

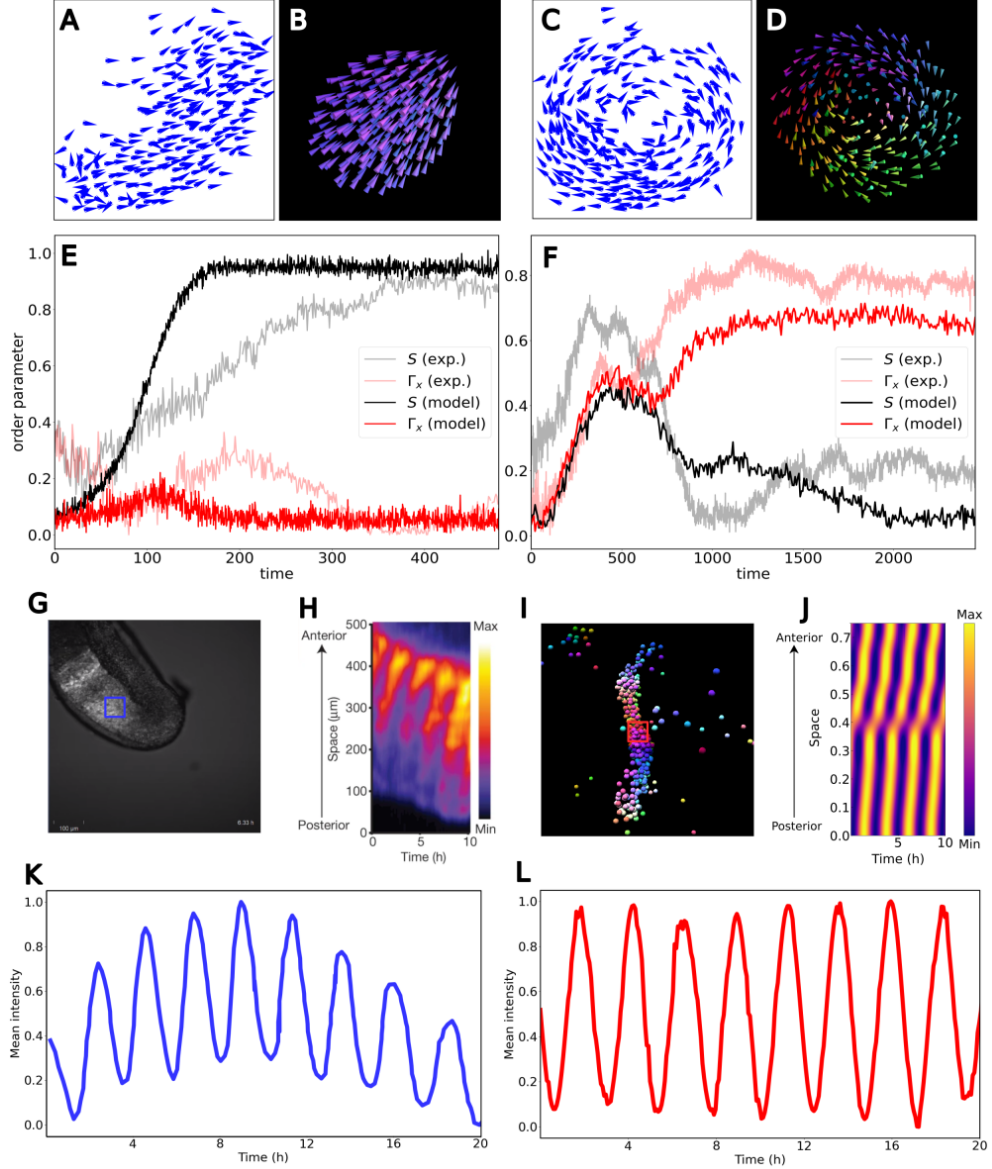


Fig. 4 Real-world parallels. (A) Experimentally observed [44] polarized (crystal) state for 300 golden shiners in a shallow water at $t = 330$. (B) Polarized state in our swarmalator model for $N = 300$, $R = 1.0$, $J = 0.7$, $\varepsilon_a = 0.9$, $\varepsilon_r = 0$. (C) Experimentally observed milling state at $t = 1450$. (D) Milling state observed in the proposed swarmalator model for $N = 300$, $R = 0.2$, $J = 0.3$, $\varepsilon_a = 0.7$, $\varepsilon_r = 0$. (E and F). Time evolution of synchronization (S) and spatial vorticity (Γ_x) order parameters characterizing polarized and milling states, respectively, from both experimental ($S(exp)$ and $\Gamma_x(exp)$), and model ($S(model)$ and $\Gamma_x(model)$) data with noise strength ($D_{x_k} = 0.005$, $D_{\sigma_k} = 0.005$). (G) In vivo fluorescence imaging and (H) kymograph of LuVeLu activity in mouse embryo, which are Fig. 1 of Ref. [47]. (I) and (J) Analogous images to (G) and (H), respectively, from the swarmalator model. Normalized mean intensity of the fluorescence quantifying the degree of the gene expression, estimated within the marked region in (G) and (I), in the mouse embryo (K) and the corresponding simulation results in (L). The parameters are $N = 500$, $R = 1.56$, $\varepsilon_a = \varepsilon_r = 0$, $J = 1.5$, $\omega = [1, 0, 0]$ with box size $3.2R$.

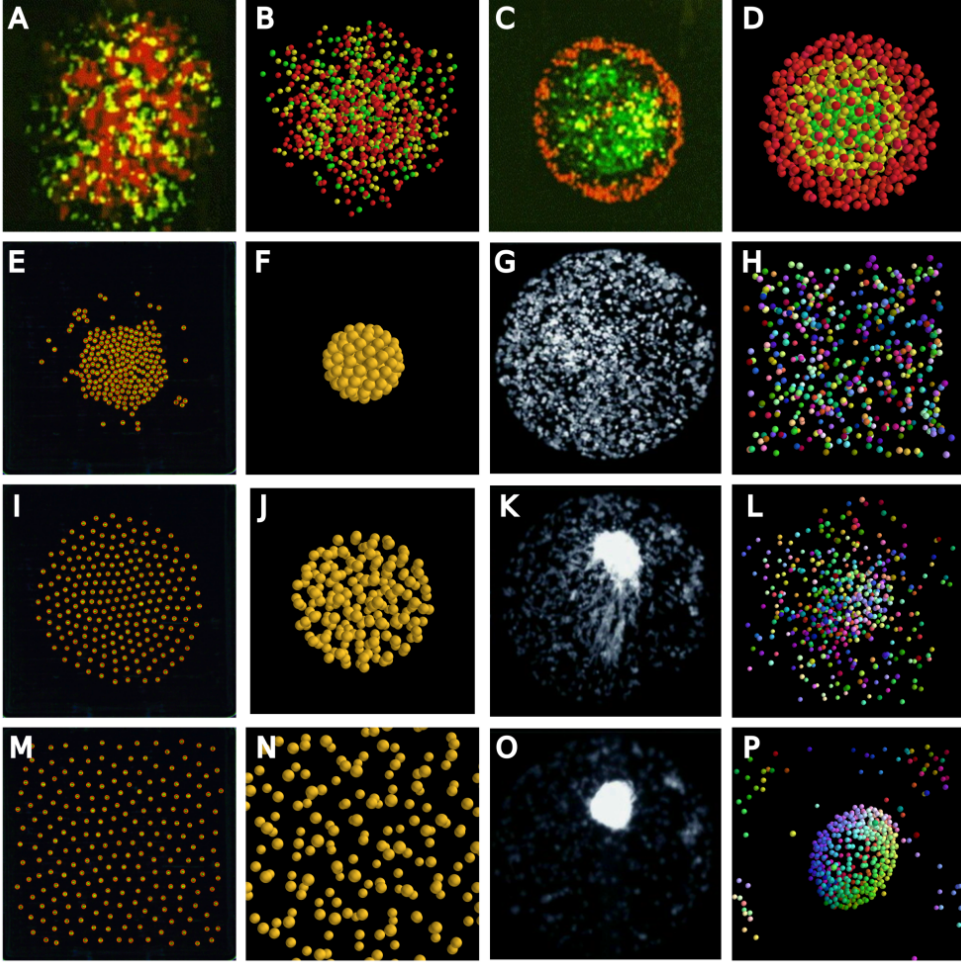


Fig. 5 Real-world parallels. Fluorescence image of (A) two types of embryonic cell mixed together and (C) aggregation of the similar types of embryonic cell, which are Figs. 4A and 4B of Ref. [49], respectively. (B and D) Phenomena similar to cell sorting is observed in the absence of phase couplings ($\varepsilon_a = 0$, $\varepsilon_r = 0$) for three populations of swarmalators. Simulation was performed with $N = 900$ with different spatial coupling among swarmalator population ($J_{11} = 0.9$, $J_{12} = 0.7$, $J_{22} = 0.2$, $J_{23} \approx 0$, $J_{33} \approx 0$, $J_{31} \approx 0$). (E, I, M) Microrobot collectives expand when rotational speed is progressively increased, which are Fig. 1 of Ref. [50]. (F, J, N) Increasingly sparse static sync state for $J < 0$ resembling the expanding microrobot collectives. (G, K, O) Snapshots illustrate the early development stages of *Dictyostelium discoideum*, dispersed cells self-aggregate to the final aggregation site, which are Fig. 1A of Ref. [52]. (H, L, P) The aggregation of swarmalators in case of local spatial interaction. Simulation performed for $N = 500$, $R = 1.4$, $J = 0.8$, $\varepsilon_a = 0$, $\varepsilon_r = 0$ with a simulation box size of $2.1R$.

Supplementary Material for Exotic swarming dynamics of high-dimensional swarmalators

Supplementary Text

S1. Derivation and features of the model

Evolution of the orientation vectors (intrinsic dynamics) of the D-dimensional swarmalator model presented in the main text is motivated by the classical Kuramoto model. In higher dimensions, the orientation vector on the unit hyper-sphere is equivalent to the phase of the classical Kuramoto model. The orientation vectors of i^{th} and j^{th} swarmalators are represented as $\boldsymbol{\sigma}_i$ and $\boldsymbol{\sigma}_j$. The sine and cosine terms involving angle ρ_{ij} subtended by the orientation vector $\boldsymbol{\sigma}_i$ on $\boldsymbol{\sigma}_j$ can be expressed in terms of orientation vectors (Fig. S1). In this setting, $\cos(\rho_{ij})$ and $\sin(\rho_{ij})$ can be expressed as $\boldsymbol{\sigma}_j \cdot \boldsymbol{\sigma}_i$ and $\boldsymbol{\sigma}_j - (\boldsymbol{\sigma}_j \cdot \boldsymbol{\sigma}_i)\boldsymbol{\sigma}_i$, respectively.

The notion of angular velocity has increased complexity in the higher dimensional Kuramoto model. In the classical Kuramoto model, the angular frequency represents rotation on a unit circle whereas in higher dimensions, the orientation vector ($\boldsymbol{\sigma}$) precesses about the angular velocity vector ($\boldsymbol{\omega}$). The phase dynamics, that is the evolution for the orientation vector, will be governed by natural frequency in the absence of the phase coupling between the swarmalators ($\varepsilon_a = \varepsilon_r = 0$). *Note that we use ‘phase dynamics’ interchangeably for ‘the evolution of the orientation vector’.* In such a scenario, the change in the orientation vector of a swarmalator after a time dt can be written as $d\boldsymbol{\sigma} = \mathbf{v}_\sigma dt$, which can be further expressed as

$$\mathbf{v}_\sigma = \boldsymbol{\omega} \times \boldsymbol{\sigma}. \quad (\text{S1})$$

Therefore in 3-dimensions,

$$\dot{\boldsymbol{\sigma}} = \boldsymbol{\omega} \times \boldsymbol{\sigma} = \begin{vmatrix} \hat{e}_1 & \hat{e}_2 & \hat{e}_3 \\ \omega_1 & \omega_2 & \omega_3 \\ \sigma_1 & \sigma_2 & \sigma_3 \end{vmatrix} = \begin{pmatrix} 0 & -\omega_3 & \omega_2 \\ \omega_3 & 0 & -\omega_1 \\ -\omega_2 & \omega_1 & 0 \end{pmatrix} \begin{pmatrix} \sigma_1 \\ \sigma_2 \\ \sigma_3 \end{pmatrix},$$

where

$$\mathbf{W} = \begin{pmatrix} 0 & -\omega_3 & \omega_2 \\ \omega_3 & 0 & -\omega_1 \\ -\omega_2 & \omega_1 & 0 \end{pmatrix}.$$

Now, the evolution equation for the orientation vector is given as

$$\dot{\boldsymbol{\sigma}} = \mathbf{W}\boldsymbol{\sigma}. \quad (\text{S2})$$

Including the effect of the attractive and repulsive interactions of the orientation vector of the swarmalators depending on their vision radius R , the evolution equation for the orientation vector corresponding to the i^{th} swarmalator is governed by

$$\dot{\boldsymbol{\sigma}}_i = \mathbf{W}_i \boldsymbol{\sigma}_i + \sum_{j=1}^N K_{ij} \left[\frac{\boldsymbol{\sigma}_j - (\boldsymbol{\sigma}_j \cdot \boldsymbol{\sigma}_i) \boldsymbol{\sigma}_i}{|\mathbf{x}_j - \mathbf{x}_i|^\gamma} \right], \quad (\text{S3})$$

where all the symbols and notations used have already been described in the model section of the main text.

S2. K -means clustering approach

Clustering is one of the interesting intrinsic feature of our model. The swarmalators self-organize to form synchronized clusters for suitable parameters. We have used the heuristic Elbow curve method [1] in K -means clustering to quantify the number of clusters.

K -means clustering is an unsupervised machine-learning algorithm that segregates data into K clusters [2, 3]. The algorithm works by randomly choosing K points called centroids and iteratively reassigning each data point to the cluster whose centroid is closer to it in terms of Euclidean distance. For further iterations, the clusters mean is taken as their new centroid. The process is repeated until the Frobenius norm of the difference in the cluster centers of two consecutive iterations is less than a threshold value.

In particular, the swarmalators are classified on the basis of their locations and phases $X = (x_1, x_2, x_3, \sigma_1, \sigma_2, \sigma_3)$ into clusters $C = \{C_1, C_2, \dots, C_K\}$.

$$\xi = \sum_{K'=1}^K \sum_{i=1}^{N_{K'}} \left| \mathbf{X}_i^{K'} - \boldsymbol{\mu}^{K'} \right|^2 \quad (\text{S4})$$

where $\boldsymbol{\mu}^{K'}$ is the center of K' cluster and ξ is the clustering error. We run the K -means clustering algorithm for our data with different values of K ranging from 1 to 20 and evaluate the clustering error or variance. The intuition is that every increment in the value of K will surely result in a decrease in variance ξ but would have diminishing returns. At some point, when the value of K crosses the true number of clusters, the diminish in returns will be significant enough that it can be seen as an ‘‘Elbow’’ in the (ξ, K) plot (see Fig. S4). The elbow point, K_{best} , can be numerically calculated by finding the maximum change of slope $\eta(K)$ in the (ξ, K) plot.

$$\eta_K = \left[\frac{\xi(K_{i-1}) - \xi(K_i)}{\xi(K_i) - \xi(K_{i+1})} \right] \quad (\text{S5})$$

$$K_{best} = \operatorname{argmax}_K (\eta_K)$$

The estimation of number of clusters from the change of slope of (ξ, K) plot is depicted in Fig. S4 for two, three and five clusters. The distinct clusters of the orientation vectors maximizes their separation due to the strong repulsive interaction among the dissimilar orientation vectors as shown in the time traces of the orientation vectors in Fig. S5.

S3. Characterization of dynamical states using the order parameters

Distinct self-organizing collective behaviors are depicted in the (J, R) phase diagram in Fig. S6A, which is Fig. 1 of the main text for $\varepsilon_a = \varepsilon_r = 0.5$, and $N = 100$. The dynamical transitions as a function of the vision radius R at three different values of $J = -0.9, 0.1$ and 0.9 , indicated as L1, L2 and L3, respectively in Fig. S6A, are depicted in Figs. S6B to S6D, respectively. The synchronization order parameter S , hollowness H , kinetic energy KE , number of clusters N_c and orientation parameter Λ including the K -means clustering are used to characterize and classify the distinct collective dynamical states. Note that $N_c \in (1, 5)$ is normalized to $N_c \in (0, 1)$, so that $N_c = 0$ corresponds to a single cluster, $N_c = 0.2$ corresponds to two-cluster and so on. In Fig. S6B, the static asynchronous region in the range of $R \in (0, 0.375]$ for $J = -0.9$ is characterized by the null value of S, KE, N_c , and a very small value of $H \approx 0.1$. Since the swarmalators are randomly oriented in the static async (SA) state, the orientation parameter also acquires $\Lambda = 0$. Sudden spike in the value of kinetic energy parameter at $R = 0.375$ elucidates the active nature of the collective state ‘active core static spiky state’ (ACSPW) in the range of $R \approx (0.375, 1.8]$. In this range of R , the values of the order parameters S, N_c and H remain very low. The orientation parameter fluctuates about $\Lambda = 0$ from positive to negative values due to the active nature of the core (see main text for explanation for the active nature of the core). Turning tube is observed for $R > 1.8$, which is characterized by a large value of S and H , whereas the parameters Λ, H and N_c acquire very low values.

In Fig. S6C, there is a transition from SA to static sync (SS) via spiky state (SP) and chimera (CH) as a function of R for $J = 0.1$. As in Fig. S6B, SA in the range of $R \in (0, 0.375]$ is characterized by near null values of all the five parameters, which manifests as SP states as R is increased further. The spiky states consists of flower and twisted states which are hollow in nature. For instance, see Fig. S7D for the hollow nature of the flower state. The hollowness parameter acquires $H \approx 1$ in the range of $R \in (0.375, 1.4]$, while the orientation parameter takes some finite value. The other parameters in this range of vision radius take very low values near zero. The SP state manifests as chimera state for $R \in (1.4, 1.8]$. As the latter state is characterized by coexisting coherent and incoherence domains (see Fig. S8), the synchronization order parameter acquires $S \in (0.2, 0.98)$ in accordance with the degree of the synchronized domain. The hollowness parameter for CH state acquires some finite but a rather low value. As R is increased further beyond $R = 1.8$, CH manifests as SS state characterized by $S = 1$. The other parameters are negligibly small in this range of R . See

Fig. S8B for the change in the synchronization order parameter S and the orientation parameter Λ as a function of R corroborating the CH and its transition to SS state.

In Fig. S6D, there is a transition from active phase wave (APW) to SS via the multi-cluster (MC) state as a function of R for $J = 0.9$ along L3. KE is rather high characterizing APW. $N_c = 0.2$ elucidates that the MC is a two-cluster state, while the finite values of the other order parameters in the MC region characterizes the nature of the cluster. For a sufficiently large R , MC manifests as SS as corroborated by a large value of the synchronization order parameter S . A schematic sketch of the distinct dynamics states observed in Fig. S6A and the order parameters used to characterize them for the competitive attractive and repulsive interactions between the orientation vectors is illustrated in Fig. S9.

S4. Spatial interaction between two swarmalators

The spatial interaction between i^{th} and j^{th} swarmalators is governed by $F_{ij} = 1 + J(\boldsymbol{\sigma}_i \cdot \boldsymbol{\sigma}_j) - 1/|\mathbf{x}_{ij}|^2$, which depends on J and $\boldsymbol{\sigma}_i \cdot \boldsymbol{\sigma}_j$. The x -intercept of the spatial interaction term F_{ij} determines the equilibrium distance between the two swarmalators, which given by $1/\sqrt{1 + J(\boldsymbol{\sigma}_i \cdot \boldsymbol{\sigma}_j)}$. $J(\boldsymbol{\sigma}_i \cdot \boldsymbol{\sigma}_j) \in [0, 1]$ for $J > 0$ along with the angle of inclination $\rho_{ij} = \cos^{-1}(\boldsymbol{\sigma}_i \cdot \boldsymbol{\sigma}_j) \in [0, \pi/2]$, and hence the x -intercept of F_{ij} lies between $[0.707, 1]$. Similarly, $J(\boldsymbol{\sigma}_i \cdot \boldsymbol{\sigma}_j) \in [0, 1]$ for $J < 0$ and $\rho_{ij} \in [\pi/2, \pi]$. In both these cases, the equilibrium distance between two swarmalators lies between $[0.707, 1]$ (see Fig. S10).

In contrast, $J(\boldsymbol{\sigma}_i \cdot \boldsymbol{\sigma}_j) \in (-1, 0]$ for $J > 0$ and $\rho_{ij} \in [\pi/2, \pi)$, and for $J < 0$ and $\rho_{ij} \in (0, \pi/2]$, in which case the equilibrium distance between two swarmalators lies between $[1, \infty)$ (see Fig. S10). Therefore, the spatial proximity between any two swarmalators depends on the value of $J(\boldsymbol{\sigma}_i \cdot \boldsymbol{\sigma}_j)$. The competitive attractive and repulsive interactions among the orientation vectors besides the vision radius R determine the value of $(\boldsymbol{\sigma}_i \cdot \boldsymbol{\sigma}_j)$ for a given J , which in turn governs the equilibrium distance between the swarmalators. This underlies the reason for the manifestation of sparse states and spatially expanding states. Further, as the two swarmalators moves out of the vision radius to establish their equilibrium distance, their orientation vectors tend to get decoherent due to repulsive interaction between. In such a scenario, for $J < 0$, the oppositely polarized orientation vectors are attracted together to minimize their spatial separation. The recursive reinforcement of such an effect of increasing and decreasing spatial proximity results in breathing state, bouncing state, pumping state, and active core state.

S5. Theoretical Analysis

S5.1 Maximal separation between two clusters

The maximal distance between the two-cluster state can be deduced in the limit of large J as follows. Let ζ_A, ζ_B be the two populations of the swarmalator collectives that form two clusters A and B , respectively. N_A, N_B be their respective cardinal

numbers. In steady state, the mean velocity of each clusters is zero and consequently, the sum of the velocities of all the swarmalators constituting the cluster A can be expressed as

$$\sum_{i \in \zeta_A} \dot{\mathbf{x}}_i = \frac{1}{N-1} \sum_{i \in \zeta_A} \sum_{j=1}^N \left[\frac{1 + J(\boldsymbol{\sigma}_i \cdot \boldsymbol{\sigma}_j)}{|\mathbf{x}_{ij}|^\alpha} - \frac{1}{|\mathbf{x}_{ij}|^\beta} \right] \mathbf{x}_{ij}. \quad (\text{S6})$$

The second summation can be explicitly expanded as intra-cluster and inter-cluster interactions as

$$\sum_{i \in \zeta_A} \sum_{j \in \zeta_A} \left[\frac{1 + J(\boldsymbol{\sigma}_i \cdot \boldsymbol{\sigma}_j)}{|\mathbf{x}_{ij}|^\alpha} - \frac{1}{|\mathbf{x}_{ij}|^\beta} \right] \mathbf{x}_{ij} + \sum_{i \in \zeta_A} \sum_{j \in \zeta_B} \left[\frac{1 + J(\boldsymbol{\sigma}_i \cdot \boldsymbol{\sigma}_j)}{|\mathbf{x}_{ij}|^\alpha} - \frac{1}{|\mathbf{x}_{ij}|^\beta} \right] \mathbf{x}_{ij} = 0. \quad (\text{S7})$$

The first term in the above summation corresponds to the interaction within the cluster A , whereas the second term in the summation corresponds to the interaction between the clusters A and B . Representing the first and second summations as A_1 and A_2 , respectively,

$$A_1 = \frac{1}{2} \sum_{i \in \zeta_A} \sum_{j \in \zeta_A, j \neq i} [\mathbf{x}_{ij} + \mathbf{x}_{ji}] \left[\frac{1 + J(\boldsymbol{\sigma}_i \cdot \boldsymbol{\sigma}_j)}{|\mathbf{x}_{ij}|^\alpha} - \frac{1}{|\mathbf{x}_{ij}|^\beta} \right] = 0. \quad (\text{S8})$$

From (S7) and (S8), $A_2 = 0$. Let D be the inter-cluster distance, such that $|x_{AB}| \approx D$.

$$\Rightarrow A_2 = \sum_{i \in \zeta_A} \sum_{j \in \zeta_B} \left[\frac{1 + J(\boldsymbol{\sigma}_i \cdot \boldsymbol{\sigma}_j)}{D^\alpha} - \frac{1}{D^\beta} \right] \mathbf{x}_{ij}.$$

Since swarmalators within both clusters A and B are synchronized, $\boldsymbol{\sigma}_i = \boldsymbol{\sigma}_A$ and $\boldsymbol{\sigma}_j = \boldsymbol{\sigma}_B \forall i \in \zeta_A$ and $j \in \zeta_B$.

$$\Rightarrow A_2 = \left[\frac{1 + J(\boldsymbol{\sigma}_A \cdot \boldsymbol{\sigma}_B)}{D^\alpha} - \frac{1}{D^\beta} \right] \sum_{i \in \zeta_A} \sum_{j \in \zeta_B} \mathbf{x}_{ij}.$$

Since $A_2 = 0$, and $\sum_{i \in \zeta_A} \sum_{j \in \zeta_B} \mathbf{x}_{ij} \neq 0$, one can obtain the inter-cluster distance as

$$D^{\beta-\alpha} = \frac{1}{1 + J(\boldsymbol{\sigma}_A \cdot \boldsymbol{\sigma}_B)}. \quad (\text{S9})$$

For the chosen values of the parameters $\alpha = 1$ and $\beta = 3$, the inter-cluster distance turns out to be

$$D = \frac{1}{\sqrt{1 + J(\boldsymbol{\sigma}_A \cdot \boldsymbol{\sigma}_B)}}. \quad (\text{S10})$$

Maximal cluster separation is obtained when $\boldsymbol{\sigma}_A \cdot \boldsymbol{\sigma}_B = -1$. Analogously, minimal cluster separation can be obtained when $\boldsymbol{\sigma}_A \cdot \boldsymbol{\sigma}_B = 1$. Accordingly, the maximal and

minimal separation between the two clusters are $D_{max} = 1/\sqrt{1-J}$ and $D_{min} = 1/\sqrt{1+J}$, respectively.

Since clusters would surely merge and synchronize once the $R > D_{max}$, the sufficient condition for emergence of static sync turns out to be $R > 1/\sqrt{1-J}$, which is numerically verified in Fig. S11A and the analytical curve matches well with the simulation results.

S5.2 Dynamics of two swarmalators

The equation of motion for the spatial dynamics for the case of two swarmalators is represented as

$$\begin{aligned}\dot{\mathbf{x}}_1 &= \{1 + J(\boldsymbol{\sigma}_1 \cdot \boldsymbol{\sigma}_2)\} \frac{\mathbf{x}_2 - \mathbf{x}_1}{|\mathbf{x}_2 - \mathbf{x}_1|^\alpha} - \frac{\mathbf{x}_2 - \mathbf{x}_1}{|\mathbf{x}_2 - \mathbf{x}_1|^\beta}, \\ \dot{\mathbf{x}}_2 &= \{1 + J(\boldsymbol{\sigma}_2 \cdot \boldsymbol{\sigma}_1)\} \frac{\mathbf{x}_1 - \mathbf{x}_2}{|\mathbf{x}_1 - \mathbf{x}_2|^\alpha} - \frac{\mathbf{x}_1 - \mathbf{x}_2}{|\mathbf{x}_1 - \mathbf{x}_2|^\beta}.\end{aligned}\quad (\text{S11})$$

The evolution equations governing the dynamics of orientation vector (internal states) is given as

$$\begin{aligned}\dot{\boldsymbol{\sigma}}_1 &= k_{12} \left[\frac{\boldsymbol{\sigma}_2 - (\boldsymbol{\sigma}_2 \cdot \boldsymbol{\sigma}_1)\boldsymbol{\sigma}_1}{|\mathbf{x}_2 - \mathbf{x}_1|^\gamma} \right], \\ \dot{\boldsymbol{\sigma}}_2 &= k_{21} \left[\frac{\boldsymbol{\sigma}_1 - (\boldsymbol{\sigma}_1 \cdot \boldsymbol{\sigma}_2)\boldsymbol{\sigma}_2}{|\mathbf{x}_1 - \mathbf{x}_2|^\gamma} \right].\end{aligned}\quad (\text{S12})$$

For spatially static steady states, $\dot{\mathbf{x}}_1 = 0$ and $\dot{\mathbf{x}}_2 = 0$, and therefore the equation of motion corresponding to the spatial dynamics can be expressed as

$$\frac{\mathbf{x}_2 - \mathbf{x}_1}{|\mathbf{x}_2 - \mathbf{x}_1|^\alpha} \left[\{1 + J(\boldsymbol{\sigma}_1 \cdot \boldsymbol{\sigma}_2)\} - \frac{1}{|\mathbf{x}_2 - \mathbf{x}_1|^{\beta-\alpha}} \right] = 0.$$

Since $(\mathbf{x}_1 - \mathbf{x}_2) \neq 0$, we get

$$|\mathbf{x}_2 - \mathbf{x}_1|^{\beta-\alpha} = \frac{1}{1 + J(\boldsymbol{\sigma}_1 \cdot \boldsymbol{\sigma}_2)}.\quad (\text{S13})$$

Substituting the above for the spatial separation between the two swarmalators in the evolution equation for the orientation vectors, the latter can be expressed only in terms of the orientation vectors as

$$\begin{aligned}\dot{\boldsymbol{\sigma}}_1 &= k [1 + J(\boldsymbol{\sigma}_1 \cdot \boldsymbol{\sigma}_2)]^{\frac{\gamma}{\beta-\alpha}} [\boldsymbol{\sigma}_2 - (\boldsymbol{\sigma}_1 \cdot \boldsymbol{\sigma}_2)\boldsymbol{\sigma}_1], \\ \dot{\boldsymbol{\sigma}}_2 &= k [1 + J(\boldsymbol{\sigma}_1 \cdot \boldsymbol{\sigma}_2)]^{\frac{\gamma}{\beta-\alpha}} [\boldsymbol{\sigma}_1 - (\boldsymbol{\sigma}_1 \cdot \boldsymbol{\sigma}_2)\boldsymbol{\sigma}_2].\end{aligned}\quad (\text{S14})$$

The above equations completely describe the static states. Note that Eq. S13 exactly turns out to be the separation between the two clusters $D = 1/\sqrt{1-J}$. Here, in the

case of two swarmalators, the sufficient condition for synchronization is exactly the same as deduced from two-cluster state. Two swarmalators can display static syc (SS), static asyc (SA) and static phase wave which cannot be distinguished from SA. In the region described by the condition $1/\sqrt{1-J} < R < 1/\sqrt{1+J}$ (see Fig. S11B), the swarmalators will have intermediate synchronization in the negative J region due to oscillations arising from the alternative synchronization and desynchronization when they enter and leave the vision radius.

S6. Attraction dominated competitive interaction between the orientation vectors

Phase diagram in the (J, R) parameter phase is depicted in Fig. S13 for $N = 100$, $\varepsilon_a = 0.9$ and $\varepsilon_r = 0.1$, to unravel the role of attraction dominated competitive interaction between the orientation vectors on the self-organizing behavior of the swarmalator collectives for the following three distinct cases:

S6.1 In the absence of angular frequency $\omega = 0$:

The phase diagram (see Fig. S13A) for this case almost resembles the phase diagram in Fig. 2 of the manuscript for purely local attractive coupling without angular frequency components. This is because of the feeble repulsive coupling strength $\varepsilon_r = 0.1$ and strong attractive coupling strength $\varepsilon_a = 0.9$, which is almost the case of local attractive coupling. The only difference is that the region of mixed synchronized state is replaced by the chimera state in Fig. S13A. Refer the main manuscript for further explanation of Fig. S13A.

S6.2 Orthogonal angular frequencies $\omega_1 \perp \omega_2$:

Half of the swarmalators collectives is distributed with $\omega_1 = [1, 0, 0]$ and other half with $\omega_2 = [0, 1, 0]$. Note that the intra-population is homogeneous, while the inter-population is heterogeneous with orthogonal angular frequencies. This figure is the same as Fig. 3 of the main manuscript. It is depicted again here to appreciate the difference in the emerging collective states (see Fig. S13B), due to the angular frequency of the orientation vectors, for the case of attraction dominated competitive interaction between the orientation vectors with that in Fig. S1A, where $\omega = 0$. The presence of the angular frequency for the orientation vectors induces active states in the phase diagram. For instance, CH is replaced by the pumping state, MC manifested as multi-cluster bouncing state (MCBS) and APW appeared as spinning spiky state (SSP). Further, the static async (SA) emerged as disordered spin (DS) state, while the static syc (SS) endowed with spin resulting establishing synchronized spinning state (SSS). *Snapshots of all these state and others observed in the two phase diagrams in the following sections are depicted in Table 1.*

S6.3 Distributed angular frequencies $\omega_1 \perp \omega_2$:

Half of the population has their angular frequency $\omega_1 = [\omega_1, 0, 0]$ randomly selected from the uniform distribution $\omega_1 \sim U(1, 3)$, while the other half have their angular frequency $\omega_2 = [0, \omega_2, 0]$ randomly selected from the uniform distribution $\omega_2 \sim U(-1, -3)$. Note that the entire swarmalator collective is characterized by heterogeneous natural frequencies. In this case, $R \in (0, 0.4)$ has only DS in the entire explored range of J (see Fig. S13C). The entire phase diagram in the region $R > 0.4$ and $J > 0$ is dominated by static multi-cluster (SMC). For $J < 0$, there is a transition from the pumping state (PS) to static embedded two-cluster (static E2C) as R is increased above 0.4. Note that most of the spinning state observed for $\omega_1 \perp \omega_2$ is disappeared in this case of distributed angular frequency due to the fact that they mutually suppress the angular precession of the orientation vectors.

S7. Competitive interaction with $\varepsilon_a = \varepsilon_r$

Now, we will investigate the effect of competitive interaction with equal attractive and repulsive coupling strengths between the orientation vectors of $N = 100$ swarmalator collectives with $\varepsilon_a = \varepsilon_r = 0.5$.

S7.1 In the absence of angular frequency $\omega = 0$:

The phase diagram depicted in Fig. S14A is exactly Fig. 1 of the main manuscript. It is depicted again here to appreciate the difference in the emerging collective states due to the angular frequency of the orientation vectors in the following. Kindly refer main text for explanation on the involved intricacies about the dynamical transitions observed in Fig. S14A. The heat maps of order parameters used to characterize the dynamical states are shown in Fig. S16.

S7.2 Orthogonal angular frequencies $\omega_1 \perp \omega_2$:

Half of the swarmalators collective is distributed with $\omega_1 = [1, 0, 0]$ and other half with $\omega_2 = [0, 1, 0]$. The swarmalator collectives result in the manifestation of several active states upon inclusion of the orthogonal angular frequencies to the orientation vectors. Disordered async (DA) is observed in the range of $R \in (0, 0.4)$ for $J \in (-1.0, 0.6)$. For $J > 0.6$ active async (AA) onsets. In the intermediate range of R , there is a transition from active core static spiky state (ACSSP) to bouncing multi-cluster (BMC) via spinning spiky state (SSP) as a function of J . For $R \approx (1.8, 2.0)$, breathing state (BS) emerges as bouncing two-cluster (B2C) via static embedded two-cluster (SE2C) as J is increased from -1.0 (see Fig. S14B).

S7.3 Distributed angular frequencies $\omega_1 \perp \omega_2$:

Half of the population has their angular frequency $\omega_1 = [\omega_1, 0, 0]$ randomly selected from the uniform distribution $\omega_1 \sim U(1, 3)$, while the other half have their angular frequency $\omega_2 = [0, \omega_2, 0]$ randomly selected from the uniform distribution $\omega_2 \sim U(-1, -3)$. Here, DS prevails in the range of $R \in (0, 0.4)$ for the entire

explored range of J . AA manifests as MC above a critical value of J in the range of $R \approx (0.4, 1.6)$ (see Fig. S14C). SE2C leads to MC for $R > 1.6$ as J is increased in the explored range of J .

S8. Repulsive dominated competitive interaction

In this section, we will unfold the effect of repulsive dominated competitive interaction between the orientation vectors of $N = 100$ swarmalator collectives with $\varepsilon_a = 0.1$ and $\varepsilon_r = 0.9$.

S8.1 In the absence of angular frequency $\omega = 0$:

The phase diagram depicted in Fig. S15A almost resembles the phase diagram in Fig. S14A for equal attractive and repulsive interactions between the orientation vectors without any frequency distributions. The two parameter space corresponding to the turning tube (TT) in Fig. S14A display breathing state (BS) and there is a small region of spinning cluster (SC) preceding the MC from the APW as R is increased from the null value.

S8.2 Orthogonal angular frequencies $\omega_1 \perp \omega_2$:

Half of the swarmalators collectives is distributed with $\omega_1 = [1, 0, 0]$ and other half with $\omega_2 = [0, 1, 0]$. In the low range of the vision radius R , disordered spin (DS) prevails in the range of $J \in (-1, 0.8)$, which manifests as AA for $J > 0.8$ (see Fig. S15B). In the range of $R \approx (0.4, 0.6)$ there is a transition from AMPW to BMC as a function of J . In the range of $R \approx (0.6, 0.1.7)$ ACSSP dominates in a rather large region of the two parameter space, which then manifests as SSP in the range of $J \approx (-0.2, 0.5)$ and finally ending up as BMC for $J > 0.5$. There is also a transition from ACSSP to BMC via spinning chimera (SCH). Finally, in the range of $R \approx (1.7, 2.0)$ there is a transition from AA→SCH→BMC and AA→BS→S2CS→BMC.

S8.3 Distributed angular frequencies $\omega_1 \perp \omega_2$:

Half of the population has their angular frequency $\omega_1 = [\omega_1, 0, 0]$ randomly selected from the uniform distribution $\omega_1 \sim U(1, 3)$, while the other half have their angular frequency $\omega_2 = [0, \omega_2, 0]$ randomly selected from the uniform distribution $\omega_2 \sim U(-1, -3)$. DS prevails in the range of $R \in (0, 0.4)$ for the entire explored range of J . AA(MC) emerges in almost entire range of R for $J < 0 (> 0)$, while there lies a small region of SE2C mediating AA and MC for $R \in (1.8, 2.0)$ as a function of J (see Fig. S15C).

S9. Local attractive coupling

The repulsive interaction between the orientation vectors are absent when $\varepsilon_r = 0$ and hence this scenario corresponds to purely local coupling among the orientation vectors. We have fixed $\varepsilon_a = 0.5$. Note that in this case, those swarmalators that lie

within the vision radius will have positive attraction between the orientation vectors, whereas those lie outside the vision radius lacks the influence of their spatial proximity on the dynamics of the orientation vectors. Hence the distributed initial conditions corresponding to the orientation vectors that lie outside R just spatially align in accordance with the evolution equation for their position vectors.

S9.1 In the absence of angular frequency $\omega = 0$:

The phase diagram in the (J, R) parameter space depicted in Fig. S17A is Fig. 2 of the main manuscript. It is depicted again here to appreciate the dynamical change in the phase diagram when angular frequencies are included to the orientation vectors.

S9.2 Orthogonal angular frequencies $\omega_1 \perp \omega_2$:

Half of the swarmalator collectives is distributed with $\omega_1 = [1, 0, 0]$ and other half with $\omega_2 = [0, 1, 0]$. Inclusion of orthogonal angular frequencies to the orientation vectors facilitates active states in most part of the phase diagram (see Fig. S17B). SA state in Fig. S17A became DS. SPW manifested as SSP, sparse SS as pumping state (PS) and very dense SS as MCBS.

S9.3 Distributed angular frequencies $\omega_1 \perp \omega_2$:

Half of the population has their angular frequency $\omega_1 = [\omega_1, 0, 0]$ randomly selected from the uniform distribution $\omega_1 \sim U(1, 3)$, while the other half have their angular frequency $\omega_2 = [0, \omega_2, 0]$ randomly selected from the uniform distribution $\omega_2 \sim U(-1, -3)$. In this case of purely local attraction, the phase diagram in Fig. S17C is exactly similar to that in Fig. S13C for the case of attraction dominated competitive interaction with distributed angular frequencies. Only difference is that the spread of the PS state in the phase diagram is reduced by increased in the spread of the static embedded two-cluster state.

S10. Global repulsive coupling

All the swarmalator collectives lie outside the vision radius of i^{th} swarmalator for $R = 0.0$ and hence this scenario corresponds to purely global repulsive coupling among the orientation vectors. We have fixed $N = 100$. Now, we will illustrate the effect of the global repulsive coupling on the swarmalator collectives in the following.

S10.1 In the absence of angular frequency $\omega = 0$:

Most of the phase diagram is dominated by the static async in the (J, ε_r) parameter space (see Fig. S18A). However, for $J > 0$ there is a transition from static async to active phase wave via static phase wave as a function of J in the range of $\varepsilon_r \in (0, 0.2)$. For $\varepsilon_r > 0.2$ and one can observe the transition from static async to active phase wave above a critical value of J .

S10.2 Orthogonal angular frequencies $\boldsymbol{\omega}_1 \perp \boldsymbol{\omega}_2$:

Half of the swarmsalators collectives is distributed with $\boldsymbol{\omega}_1 = [1, 0, 0]$ and other half with $\boldsymbol{\omega}_2 = [0, 1, 0]$. SA in the previous case manifests as disordered spin (DS) in the presence of two populations of swarmsalators with mutually perpendicular angular frequencies (see Fig. S18B). APW and SPW becomes spinning spiky states (SSP).

S10.3 Distributed angular frequencies $\boldsymbol{\omega}_1 \perp \boldsymbol{\omega}_2$:

Half of the population has their angular frequency $\boldsymbol{\omega}_1 = [\omega_1, 0, 0]$ randomly selected from the uniform distribution $\omega_1 \sim U(1, 3)$, while the other half have their angular frequency $\boldsymbol{\omega}_2 = [0, \omega_2, 0]$ randomly selected from the uniform distribution $\omega_2 \sim U(-1, -3)$. The entire phase diagram is occupied only by disordered spin because of purely global repulsion and heterogeneous nature of the natural frequencies of the orientation vectors (see Fig. S18C).

*S11. Extended model for school of fish In this section, we extend our model to capture the self-organizing behaviors of school of fish by including the self-propulsion velocity and slightly modifying the phase repulsive interaction. The orientation vector describing the internal state of a swarmsalator can be interpreted as the heading direction of the swarmsalator (fish), which is a typical characteristic feature of school of fish during their bait-ball or milling behavior [4]. These collective behaviors offer several advantages such as enhanced predator defense and increased foraging efficiency [5]. We choose the self-propulsion velocity along the orientation of the agent as

$$\mathbf{v}_i = c_i \boldsymbol{\sigma}_i, \quad (\text{S15})$$

where, c_i is the mapping coefficient for self-propulsion velocity. Hence the spatial dynamics in Eq. (1) of the main text can be modified as

$$\dot{\mathbf{x}}_i = c_i \boldsymbol{\sigma}_i + \frac{1}{N-1} \sum_{j=1}^N \left[\{1 + J(\boldsymbol{\sigma}_i \cdot \boldsymbol{\sigma}_j)\} \frac{\mathbf{x}_j - \mathbf{x}_i}{|\mathbf{x}_j - \mathbf{x}_i|^\alpha} - \frac{\mathbf{x}_j - \mathbf{x}_i}{|\mathbf{x}_j - \mathbf{x}_i|^\beta} \right]. \quad (\text{S16})$$

Bait-ball or milling of school of fish maintains their social boundary with some radius L with respect to their center of mass. During schooling, fishes maneuver their orientation such that they stay inside this social structure (L) to increase their chance of survival [6]. The evolution equation corresponding to the orientation vector can be represented as

$$\dot{\boldsymbol{\sigma}}_i = \mathbf{W}_i \boldsymbol{\sigma}_i + \sum_{j=1}^N \frac{\varepsilon_a}{N_i} \left[\frac{\boldsymbol{\sigma}_j - (\boldsymbol{\sigma}_j \cdot \boldsymbol{\sigma}_i) \boldsymbol{\sigma}_i}{|\mathbf{x}_j - \mathbf{x}_i|^\gamma} \right] - \mathbf{F}_i. \quad (\text{S17})$$

Note that the $\boldsymbol{\omega}_i = 0$ and the repulsive coupling among the orientation vectors in Eq. (1) of the main text is replaced by the term \mathbf{F}_i , which is expressed as

$$\mathbf{F}_i = \frac{\mathbf{x}_i^c - (\mathbf{x}_i^c \cdot \boldsymbol{\sigma}_i) \boldsymbol{\sigma}_i}{|L \hat{\mathbf{x}}_i^c - \mathbf{x}_i^c|}, \quad (\text{S18})$$

where $\mathbf{x}_i^c = \mathbf{x}_i - \mathbf{x}_c$ represents the position of i^{th} swarmalator with respect to their center of mass $\mathbf{x}_c = \sum_{i=1}^N \mathbf{x}_i / N$. The term \mathbf{F}_i can be considered as the force that enforces the centripetal inclination of the school of fish which facilitates them to maintain the dense bait-ball formation to evade their predators [7].

To describe the observed collective behaviors of school of fish, we use three order parameters, namely synchronization parameter (S), spatial vorticity (Γ_x), and phase vorticity (Γ_σ). The synchronization parameter provides the measurement of the alignment of individuals in the group. To measure the rotational motion of the fishes, we use two vorticity parameters [4]. Spatial vorticity (Γ_x) is calculated using spatial velocity and is useful for capturing the vorticity arising due to the lateral motion, while the phase vorticity is calculated using the orientation vectors and is useful for measuring the vorticity due to motion along the heading direction. The spatial vorticity is defined as

$$\Gamma_x = \frac{1}{N} \left| \sum_i^N \hat{\mathbf{x}}_i^c \times \hat{\mathbf{v}}_i \right|, \quad (\text{S19})$$

where, $\hat{\mathbf{x}}_i^c$ is the unit vector corresponding to the position vector of the i^{th} swarmalator with respect to their center of mass \mathbf{x}_c and $\hat{\mathbf{v}}_i$ is the unit vector of the spatial velocity of the i^{th} swarmalator. Phase vorticity is defined as

$$\Gamma_\sigma = \frac{1}{N} \left| \sum_i^N \hat{\mathbf{x}}_i^c \times \boldsymbol{\sigma}_i \right|. \quad (\text{S20})$$

Both vorticity parameters, Γ_x and Γ_σ , can vary in the range 0 to 1. Typical configurations observed during the schooling of fish are the swarm state, polarized state, and milling state. In the case of milling, swarmalators, here fishes, show coordinated rotational motion and in polarized (crystal) state fishes are aligned. Quantitatively, the milling state is characterized by high vorticity ($\Gamma_x \approx 1, S \approx 0$), while the polarized state is characterized by the high value of synchronized parameters ($S \approx 1, \Gamma_x \approx 0$). In the swarm state, the fish are neither ordered nor form vorticity and hence this state is characterized by a feeble spatial and phase vorticities ($\Gamma_x \approx 0, \Gamma_\sigma \approx 0$) and negligible value of the synchronization order parameter ($S \approx 0$). The collective states observed in the modified model (Eq. S16, Eq. S17) and the time evolution of the above order parameters are depicted in Fig. S19. Heat maps of the order parameters in (J, R) space are shown in Fig. S20 and Fig. S21.

S12. Extended model for cell sorting

In the swarmalator model, the orientation vectors can be used to represent different types of cells. Similar types of cells tend to cluster together due to the different adhesive properties. This behavior can be captured by considering two or more populations of swarmalators with different spatial coupling. We assume that the state of the cell is not changing during the sorting process and hence $\varepsilon_a = \varepsilon_r = 0$. Since $\boldsymbol{\omega} = 0$, the evolution equations of motion for three populations of swarmalators governing the cell

sorting dynamics can be given as

$$\dot{\mathbf{x}}_i^{(b)} = \mathbf{v}_i^{(b)} + \sum_{b'=1}^3 \frac{1}{(N^{(b')} - \delta_{bb'})} \sum_{j=1}^N \left[1 + J^{(bb')} (\boldsymbol{\sigma}_i^{(b)} \cdot \boldsymbol{\sigma}_j^{(b')}) \frac{\mathbf{x}_j^{(b')} - \mathbf{x}_i^{(b)}}{|\mathbf{x}_j^{(b')} - \mathbf{x}_i^{(b)}|^\alpha} - \frac{\mathbf{x}_j^{(b')} - \mathbf{x}_i^{(b)}}{|\mathbf{x}_j^{(b')} - \mathbf{x}_i^{(b)}|^\beta} \right] \quad (\text{S21})$$

where $b = 1, 2$ and 3 corresponds to the three distinct population of cells A, B and C , respectively. We have assumed type- A (B) cells have more adhesiveness than type- B (C) and hence accordingly, $J^{AA} > J^{AB} > J^{BB} > J^{BC} > J^{CC} > J^{AC} = 0$, where $J^{AB} = J^{BA}$, $J^{AC} = J^{CA}$, and $J^{BC} = J^{CB}$.

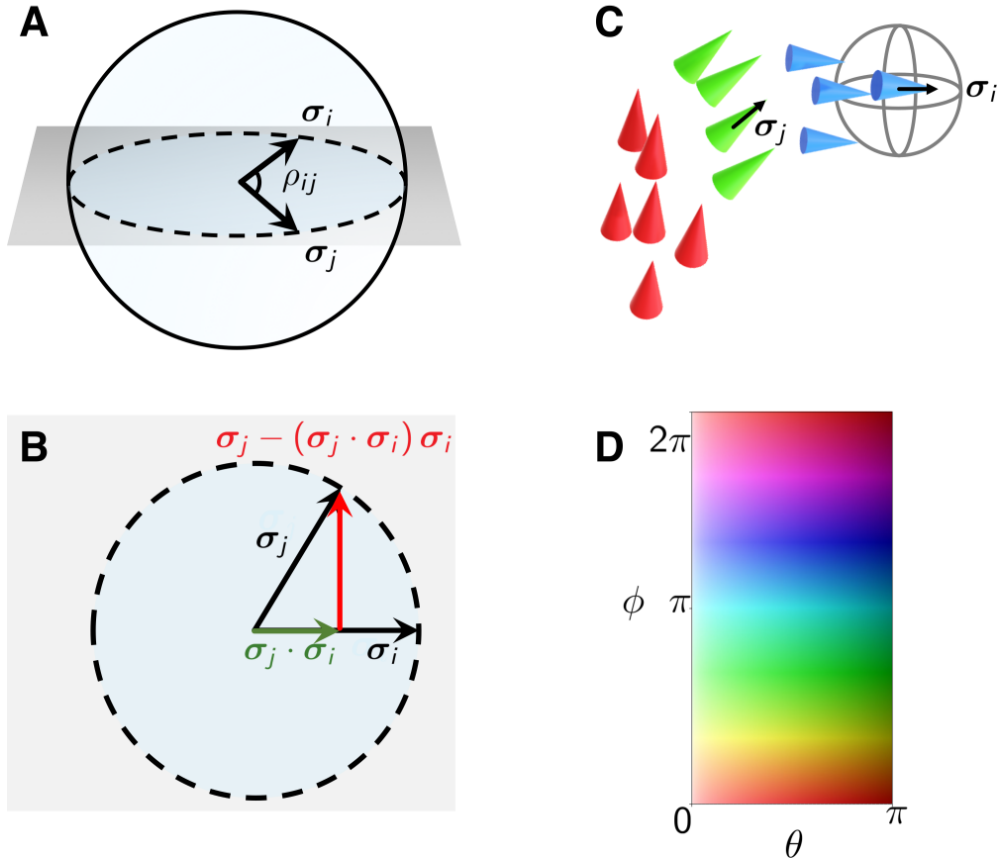


Fig. S1 Deriving 3D phase mathematical model and its visualisation. (A) Orientations σ_i and σ_j of i^{th} and j^{th} swarms, respectively, can be represented as vectors pointing on a unit sphere. (B) Deriving the analogues of $\sin(\rho_{ij})$ and $\cos(\rho_{ij})$ in terms of orientation vectors σ_i and σ_j . Here ρ_{ij} is the angle of inclination of orientation vectors, $\cos(\rho_{ij})$ is simply the projection of σ_j on σ_i , $\sin(\rho_{ij})$ is the y -component of σ_j . (C) Each swarm is represented by a cone with its apex pointing along its orientation vector. (D) The heat map, encoding the degree of orientation of the vectors which in turn is determined by the polar angle (θ) and the azimuthal angle (ϕ), is used to color the cones in accordance with the distribution of the initial conditions, which facilitates to identify distinct collective states even when the cones are masked behind a dense set of cones.

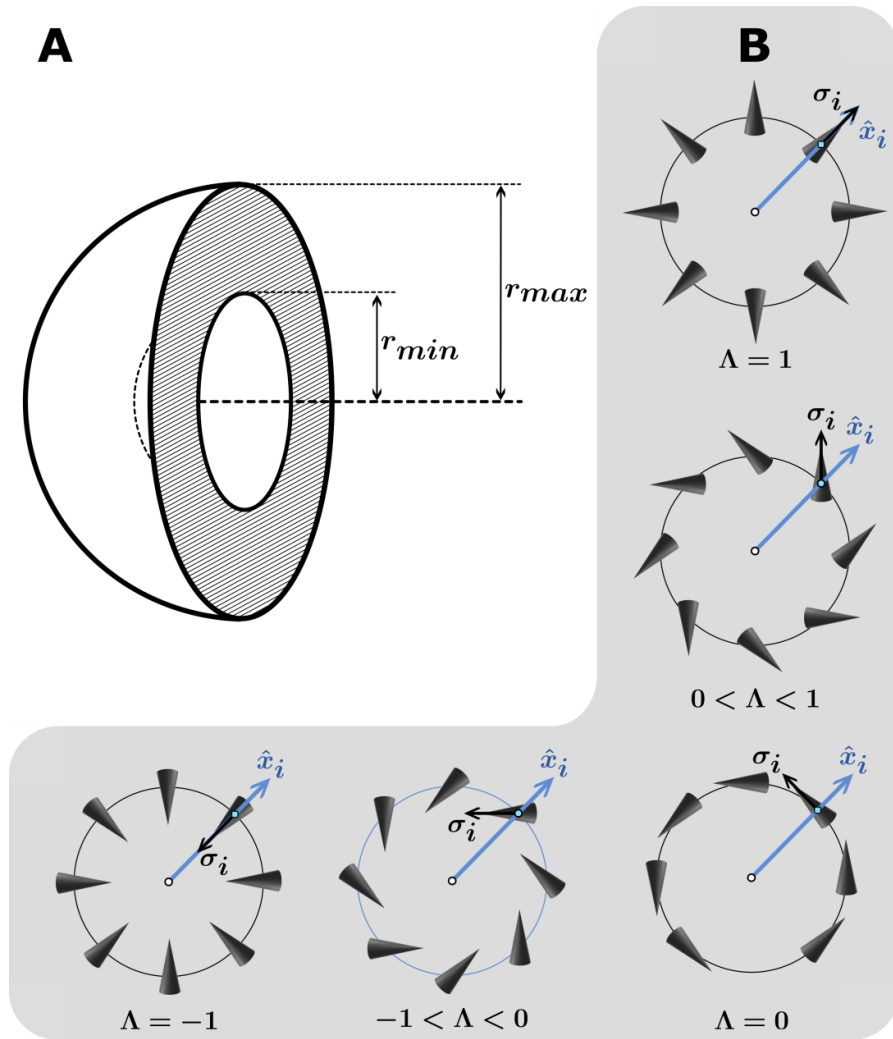


Fig. S2 Schematic diagram to facilitate the deduction of hollowness and orientation parameters. (A) For hollow states, the radius of the hollow cavity is denoted by r_{min} , and the total radius of the spherical state is denoted by r_{max} . The ratio between r_{min} and r_{max} determines the degree of hollowness. (B) The blue arrow \hat{x}_i represents the position from the center and the black arrows σ_i represent the orientation of i^{th} swarmalator. The angle between the position vector and the orientation vectors of the i^{th} swarmalator determines its degree of alignment.

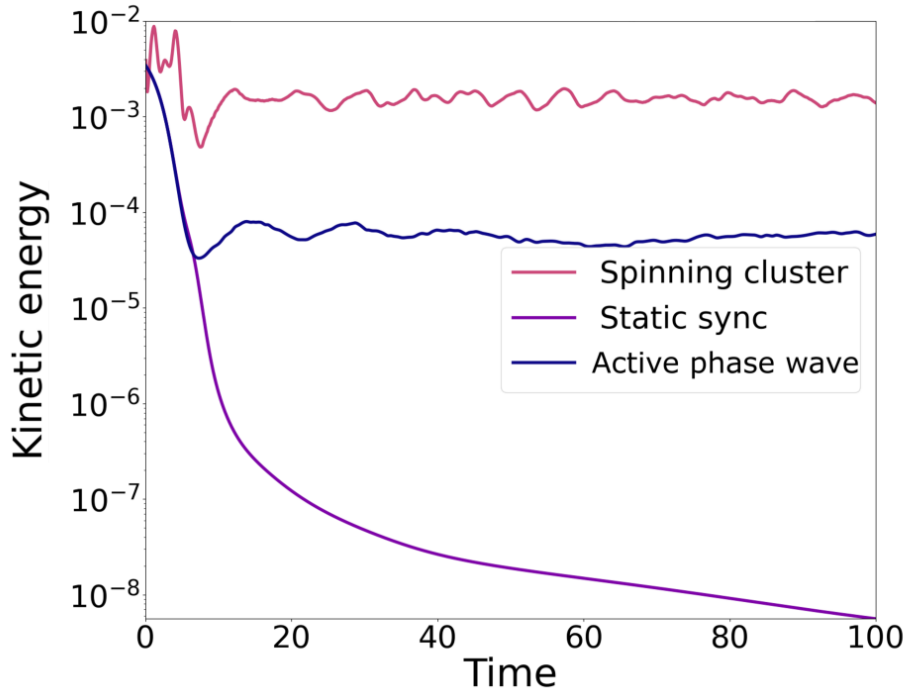


Fig. S3 Time evolution of the kinetic energy parameter. Time evolution of the kinetic energy parameter corresponding to the static sync (SS) for $J = 0.1, \varepsilon_a = \varepsilon_r = 1.0, N = 200$ and $r = 2$, active phase wave (APW) for $J = 0.75, \varepsilon_a = \varepsilon_r = 1.0, N = 200$ and $R = 0$, and the spinning cluster state for $J = 1.0, \varepsilon_a = 0.0, \varepsilon_r = 1.0, N = 200$ and $R = 0.5$. The spinning cluster can be seen in the Movie S21, as its spinning nature is difficult to perceive in the snapshot. The initial peak in the kinetic energy parameter is due to the transient dynamics. The value of the kinetic energy parameter for the spinning cluster state is an order of magnitude greater than for the active phase wave.

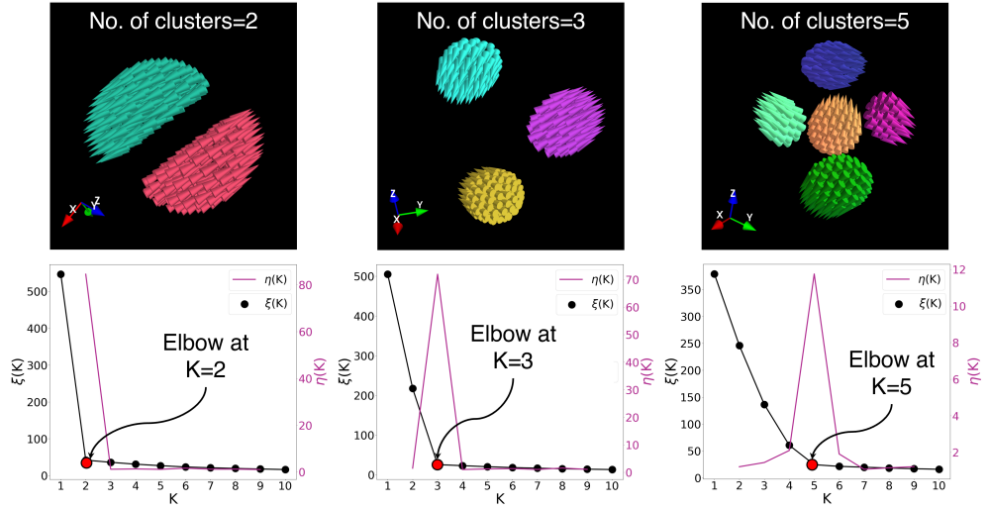


Fig. S4 Estimation of number of clusters using K -means clustering. The diagram illustrates the implementation of the K -means clustering framework (discussed in the supplementary text S2) to estimate the number of clusters in the ‘multi-cluster states’. The number of clusters can be found using the elbow method from the (ξ, K) phase plot. The black line corresponds to the error $\xi(K)$ whereas the red line corresponds to the change of slope function $\eta(K)$. The elbow is the point where the change of slope is maximum, seen as a peak in the red curve. For $K = 2$ case, half of the peak is not visible since the change of peak function is defined only for $K \geq 2$. The elbow of $\xi(K)$ and the peak of $\eta(K)$ in the bottom row clearly quantify two, three and five clusters observed in the respective column of the first row (refer supplementary text S2 for more details).

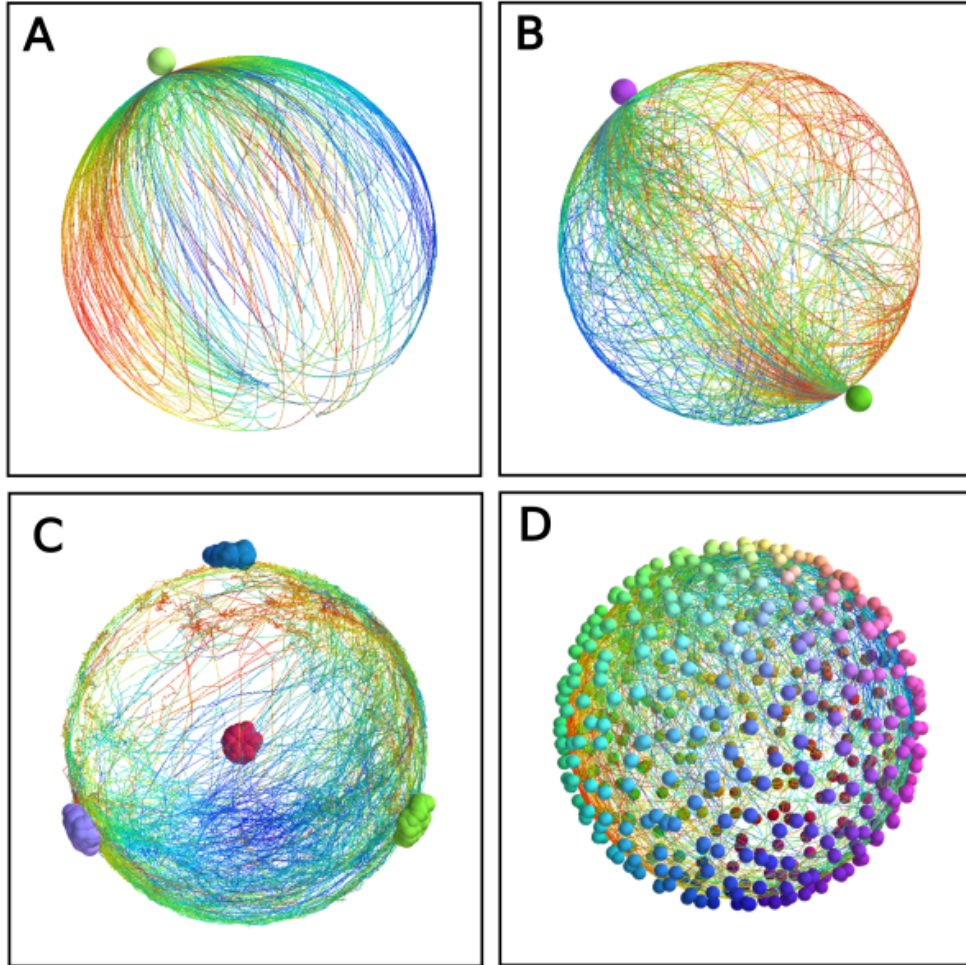


Fig. S5 Time traces of the orientation vectors. Time traces of the orientation vectors corresponding to $N = 200$ swarms. The colored spheres, colored according to the heat map in Fig. S1, are the asymptotic clusters of the orientation vectors. **(A)** Single cluster for $R = 2$. **(B)** Two-cluster for $R = 1$. **(C)** Four-cluster for $R = 0.25$. **(D)** Orientations for Twisted (Spiky) state. The values of the other parameters are $\varepsilon_a = \varepsilon_r = 0.6$ and $J = 0.8$. The distinct clusters of the orientation vectors maximizes their spatial separation due to the strong repulsive interaction among the dissimilar orientation vectors/clusters.

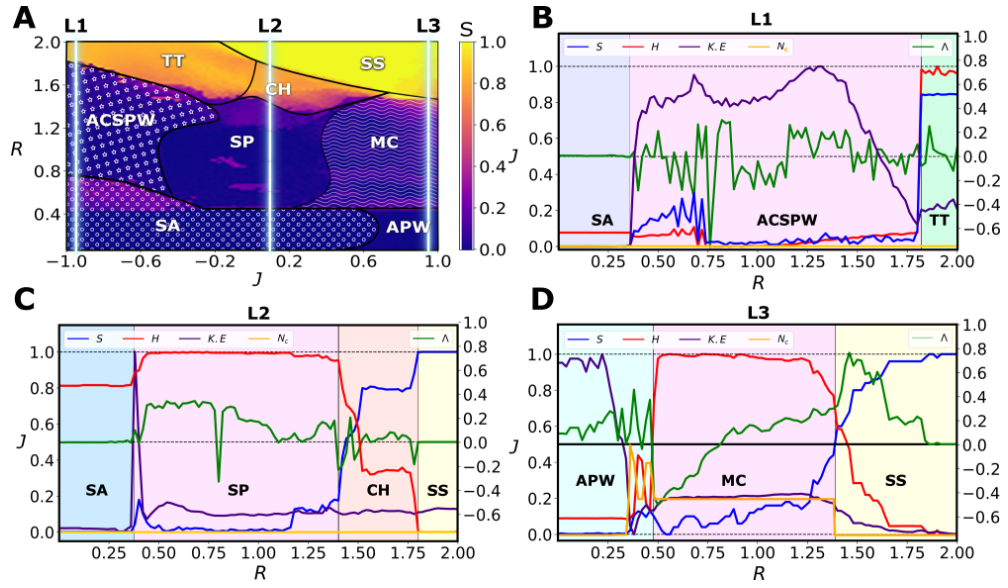


Fig. S6 Dynamical transition using the order parameters. (A) Fig. 1 of the main text for $\varepsilon_a = \varepsilon_r = 0.5$, and $N = 100$. The dynamical transitions leading to distinct self-organizing collective behaviors as a function of the vision radius R at three different values of $J = -0.9, 0.1$ and 0.9 (indicated as L1, L2 and L3, respectively) are depicted in Figs. (B-D), respectively. The synchronization order parameter S , hollowness H , kinetic energy KE , number of cluster N_c and orientation parameter Λ are used to characterize and distinguish distinct dynamical states. Refer supplementary text S3 for brief explanation on characterizing the distinct dynamical transitions (states) using the order parameters.

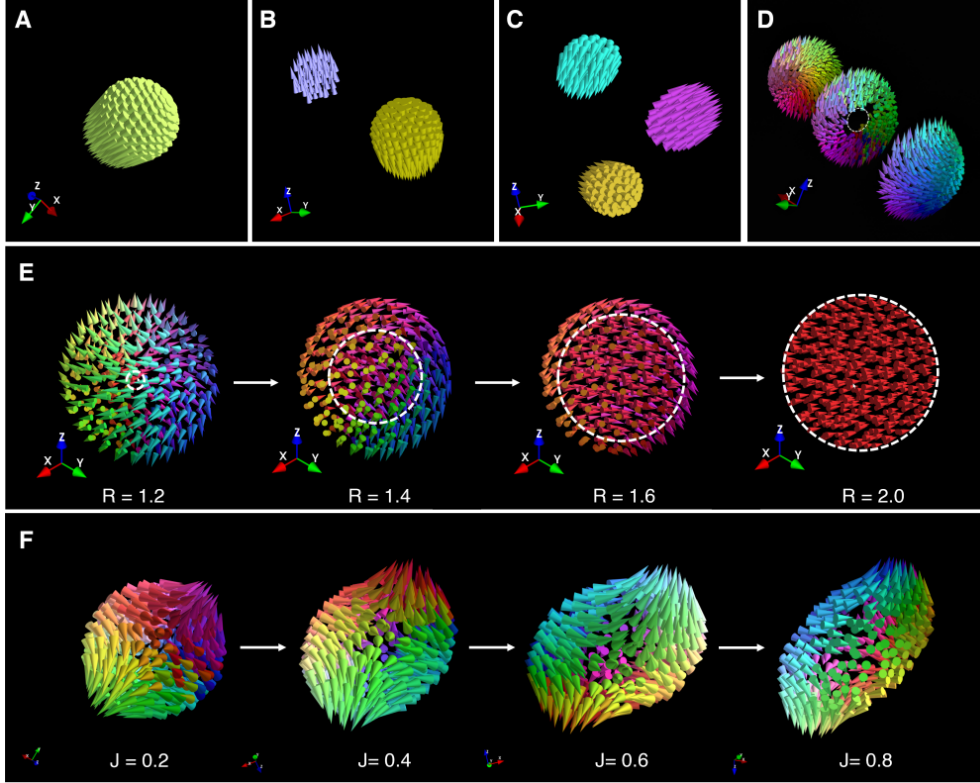


Fig. S7 Cluster states and the manifestation of chimera. We fix $N = 500$. **(A)** Static synchronized state (single cluster) for $R = 2$. **(B)** Two-cluster for $R = 1$. **(C)** Three-cluster for $R = 0.5$. The other parameters are $\varepsilon_a = \varepsilon_r = 0.5$. **(D)** A 3D-slice plot of Flower state to illustrate the spherical cavity at its core. These states are already depicted in Fig. 1 of the main manuscript $\varepsilon_a = \varepsilon_r = 0.5$. **(E)** Simulation results for $J = 0, \varepsilon_a = \varepsilon_r = 1$. Since $J = 0$ the spatial dynamics are independent of the orientation vectors of the swarmalators, but competitive interactions among the orientation vector exists due to non-zero values of ε_a and ε_r . Manifestation of chimera state can be observed during the transition from the twisted state (SP) to the static sync (SS) state as the vision radius is increased. It is evident that as R increases the coherent core increases in size enveloped by static phase wave finally resulting in completely synchronized state. **(F)** Flower state for $R = 1.0, \varepsilon_a = \varepsilon_r = 0$, the cluster elongates when the value of parameter J is increased. Similarly aligned swarmalators will be attracted strongly in proportion to the value of J . When J is small or zero, the effect of similarity of the orientation vectors on the spatial proximity is absent, and the swarmalators settle on to a unit sphere. Increasing J will make the swarmalators near the two poles (places where the symmetry axis passes through the sphere) come closer, hence distorting the spherical shape. Some of these states are already depicted in Fig. 1 of the main manuscript for $\varepsilon_a = \varepsilon_r = 0.5$. Here the collective states are depicted for $N = 500$ swarmalators and scaled up for better perception of the distinct self-organizing collective states.

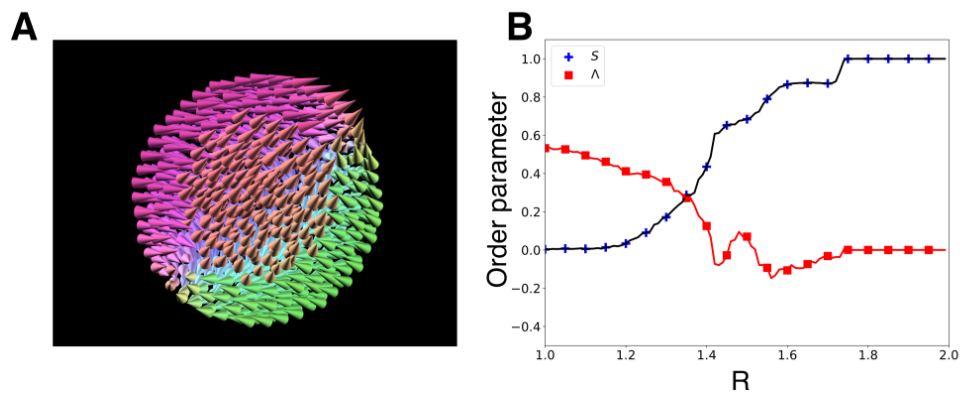


Fig. S8 The 3D cross-section of the chimera. (A) Illustration of coherent and incoherent domains constituting chimera. The static sync core and the phase wave shell surrounding it are clearly illustrated. The transition between the two layers is sharp, suggesting that there is an explosive transition to synchronization governed by the distance-dependent interaction. (B) The synchronization order parameter S and orientation parameter Λ are depicted as a function of the vision radius R . As R is increased S increases characterizing the degree of synchronized core and eventually reaching unity elucidating the emergence of SS. Note that Λ decreases as the orientation vectors align among themselves and eventually attains the null value when the static sync onsets characterizing the emergence of complete coherence among the orientation vectors.

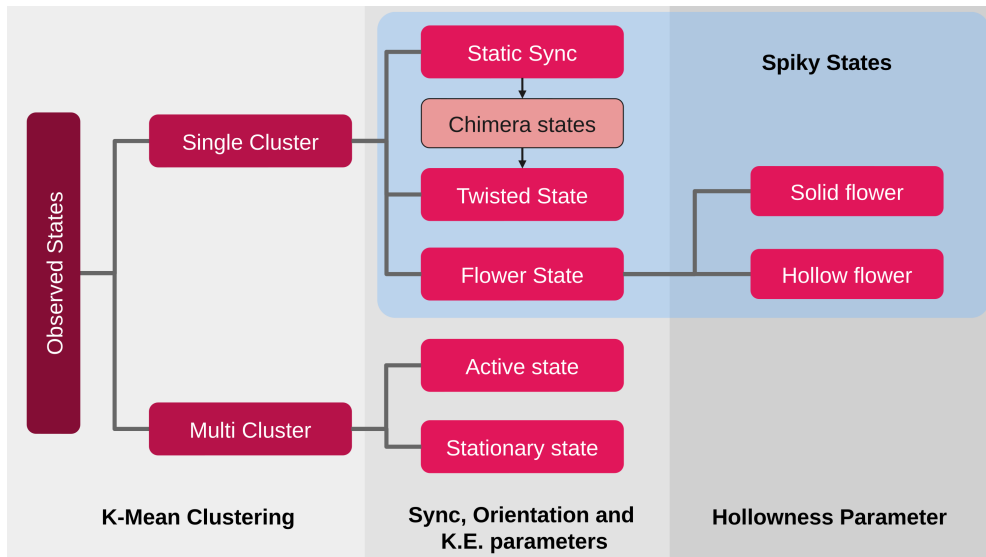


Fig. S9 Schematic sketch of the self-organizing states for competitive interaction. We have observed a variety of self-organizing collective dynamics states in our model for a different set of parameters. The schematic diagram shows the distinct states observed across the different ranges of parameters for $\omega = 0$ and $\varepsilon_a = \varepsilon_r = 0.5$, which are characterized and classified based on the values of the five distinct order parameters namely, synchronization order parameter S , hollowness H , kinetic energy KE , number of cluster N_c and orientation parameter Λ .

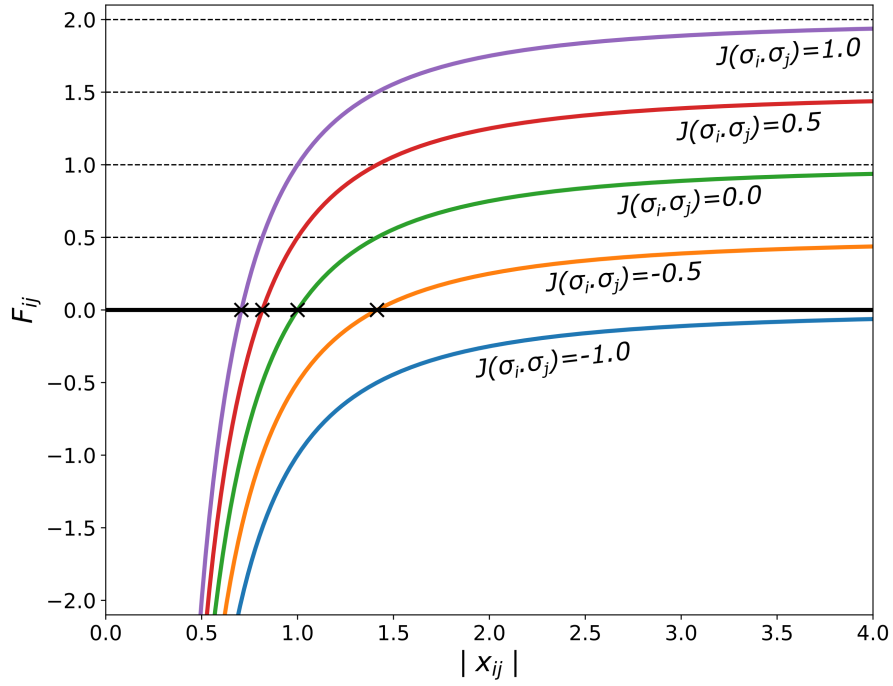


Fig. S10 Spatial interaction between two swarmalators i and j . The x -intercept of the spatial interaction term $F_{ij} = 1 + J(\boldsymbol{\sigma}_i \cdot \boldsymbol{\sigma}_j) - 1/|\mathbf{x}_{ij}|^2$ determines the equilibrium distance between the i^{th} and j^{th} swarmalators, given by $1/\sqrt{1 + J(\boldsymbol{\sigma}_i \cdot \boldsymbol{\sigma}_j)}$. It is evident that the equilibrium distance between any two swarmalators can vary from 0.707 to ∞ depending on the value of J and the dot product of $\boldsymbol{\sigma}_i$ and $\boldsymbol{\sigma}_j$. Refer supplementary text S4 for more discussions on the effect of the spatial interaction term on the observed collective dynamical states.

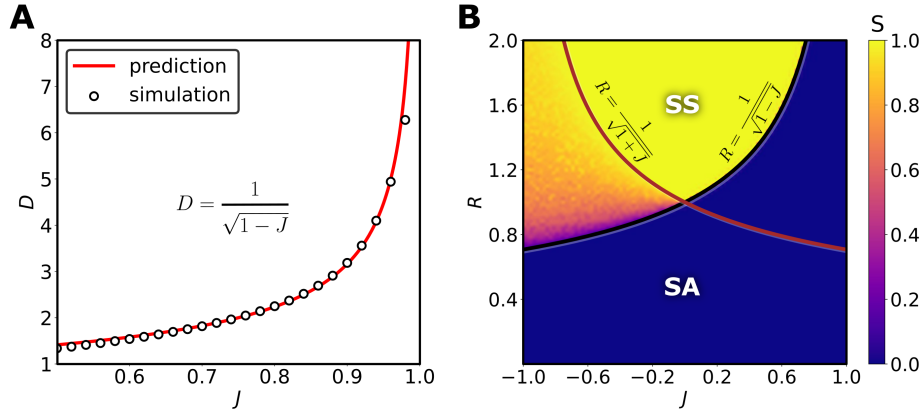


Fig. S11 Dynamics of two swarmalators. **A.** Cluster separation of two-cluster state with varying J . The solid red line is the analytical prediction and the circular markers are the simulated results. **B.** Dynamics of swarmalator model for $N=2$ with equal attractive and repulsive interactions among the orientation vectors. Heat map illustrates the synchronization order parameter estimated from the evolution of the orientation vectors. The sufficient condition for synchronization was shown to be $R > |\mathbf{x}_{12}| = 1/\sqrt{1+J(\boldsymbol{\sigma}_1 \cdot \boldsymbol{\sigma}_2)}$ in Sec. S6. The analytical critical curve $R = 1/\sqrt{1 \pm J}$, depicted in the figure, matches fairly with the simulation results.

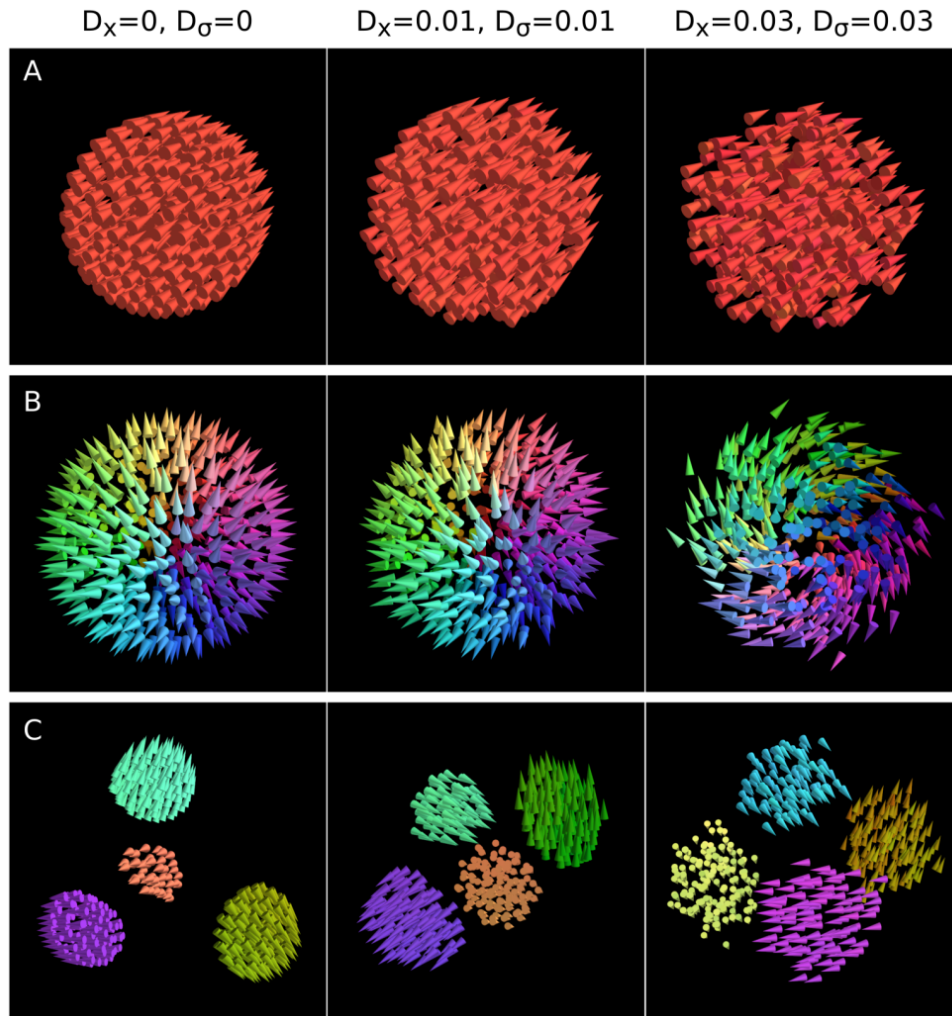


Fig. S12 Effect of noise on the dynamical states. The figure demonstrates the effect of the white noise for increasing noise strength ($D_x = D_\sigma = 0.00, 0.01$ and 0.03). Note that here same value for the noise strength was used for all x, y, z components of D_x and D_σ . **(A)** Static sync state. **(B)** Spiky state. **(C)** Cluster state. It is evident that all these three states are quite robust against the noise. Note that all the other reported collective dynamical states are also found to be robust against the employed degree of the noise.

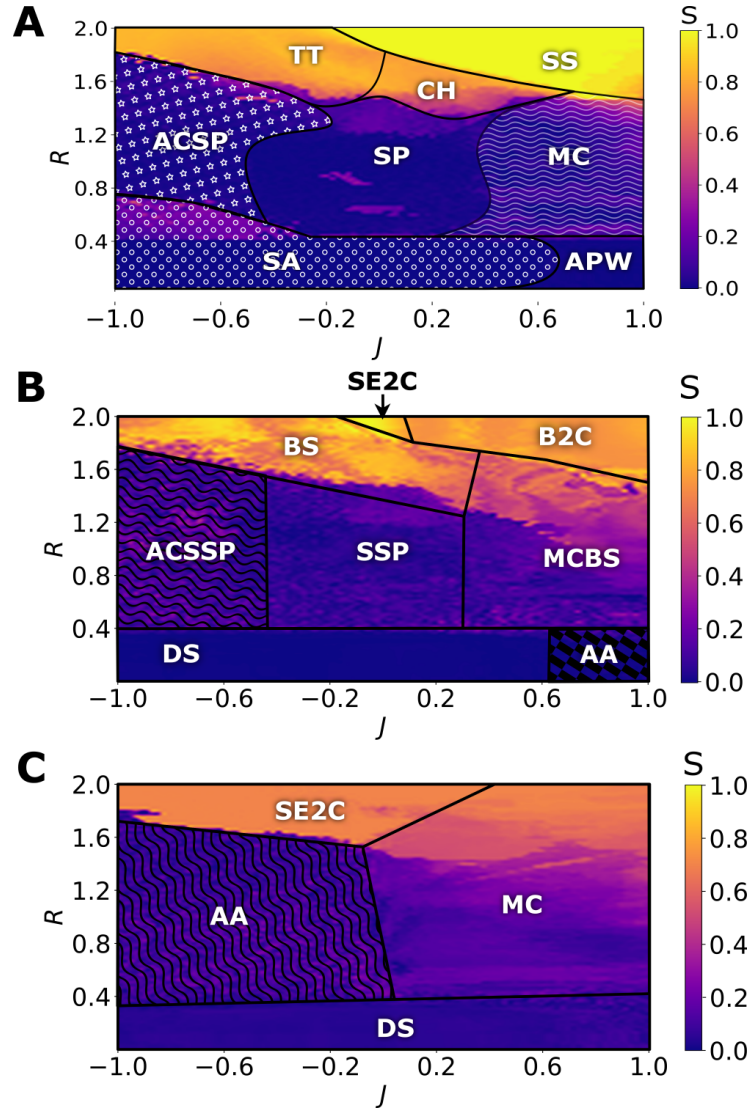


Fig. S14 Competitive interaction with equal attractive and repulsive coupling strengths. Phase diagram in the (J, R) parameter space for $N = 100$ swarmalator collectives when $\varepsilon_a = \varepsilon_r = 0.5$. (A) In the absence of angular frequency $\omega = 0$. (B) Orthogonal angular frequencies $\omega_1 \perp \omega_2$. (C) Distributed orthogonal angular frequencies $\omega_1 \perp \omega_2$. The self-organizing emergent states observed in the depicted phase diagrams are static async (SA), active phase wave (APW), multi-cluster (MC), spiky state (SP), active core static spiky state (ACSPW), turning tube (TT), chimera (CH), synchronized states (SS), disordered spin (DS), active async (AA), bouncing multi-cluster (BMC), spinning spiky states (SSP), active core spinning spiky state (ACSSP), breathing state (BS), bouncing two-cluster state (B2C), and static embedded two-cluster (Static E2C).

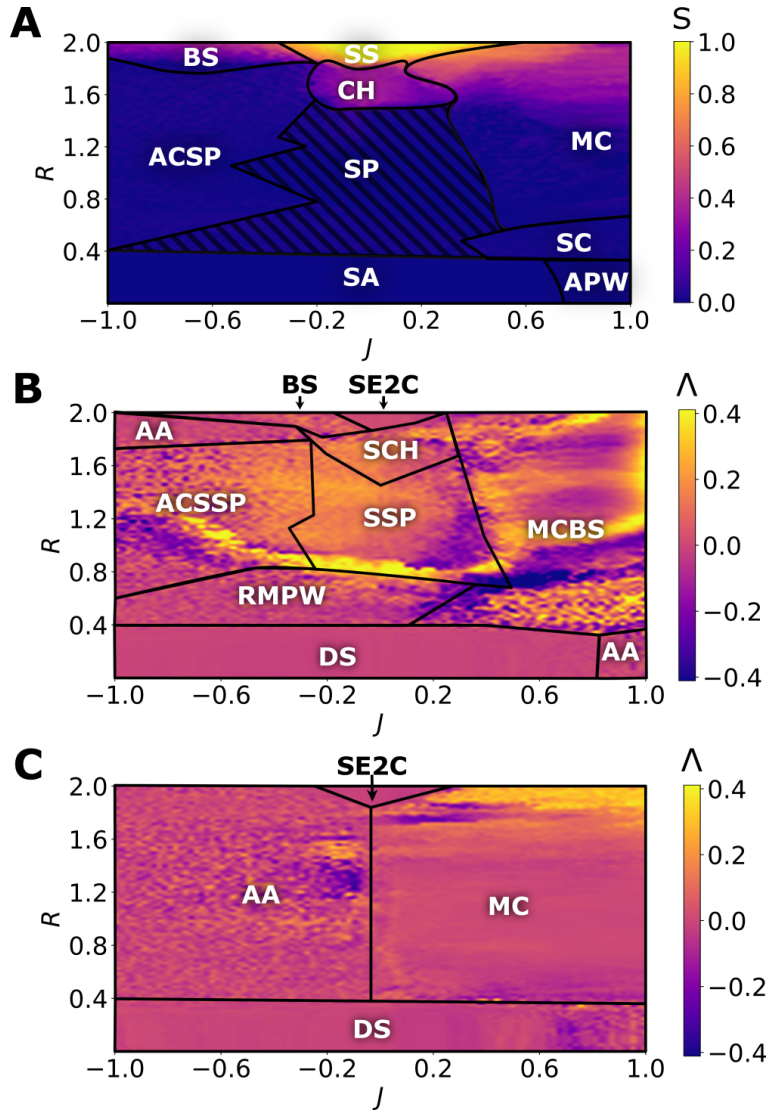


Fig. S15 Repulsion dominated competitive interaction. Phase diagram in the (J, R) parameter space for $N = 100$ swarms when $\varepsilon_a = 0.1$ and $\varepsilon_r = 0.9$ (A) In the absence of angular frequency $\omega = 0$. (B) Orthogonal angular frequencies $\omega_1 \perp \omega_2$. (C) Distributed orthogonal angular frequencies $\omega_1 \perp \omega_2$. The self-organizing emergent states observed in the depicted phase diagrams are static async (SA), active phase wave (APW), spinning cluster (SC), multi-cluster (MC), spiky state (SP), active core static spiky state (ACSPW), breathing state (BS), chimera (CH), synchronized states (SS), disordered spin (DS), active async (AA), bouncing multi-cluster (BMC), spinning spiky states (SSP), active core spinning spiky state (ACSSP), static two-cluster (S2CS), spinning chimera (SCH), attractive mixed phase wave (AMPW), and static embedded two-cluster (Static E2C).

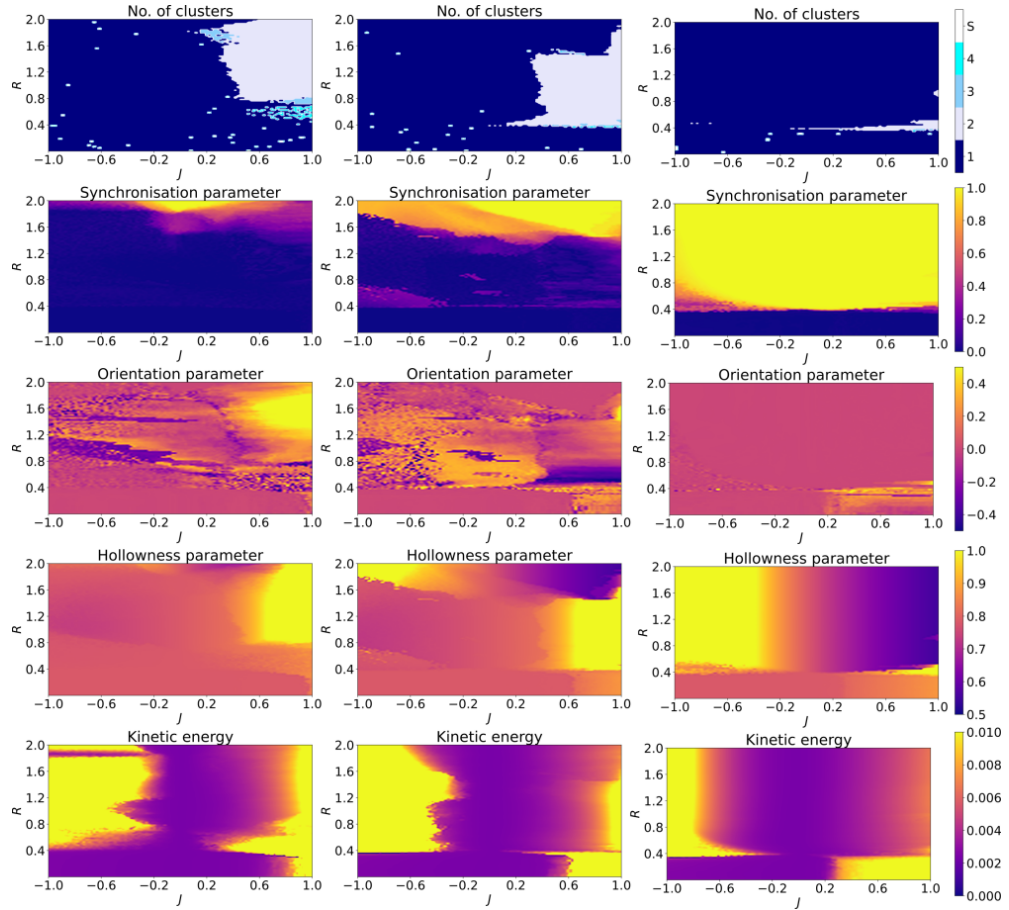


Fig. S16 Heat maps of the order parameters for competitive interaction. Heat maps in (J, R) parameter space for $N = 100$ swarmalator collectives for $\varepsilon_a = \varepsilon_r = 0.5$ of all the order parameters used to characterize distinct dynamical states in the phase diagrams.

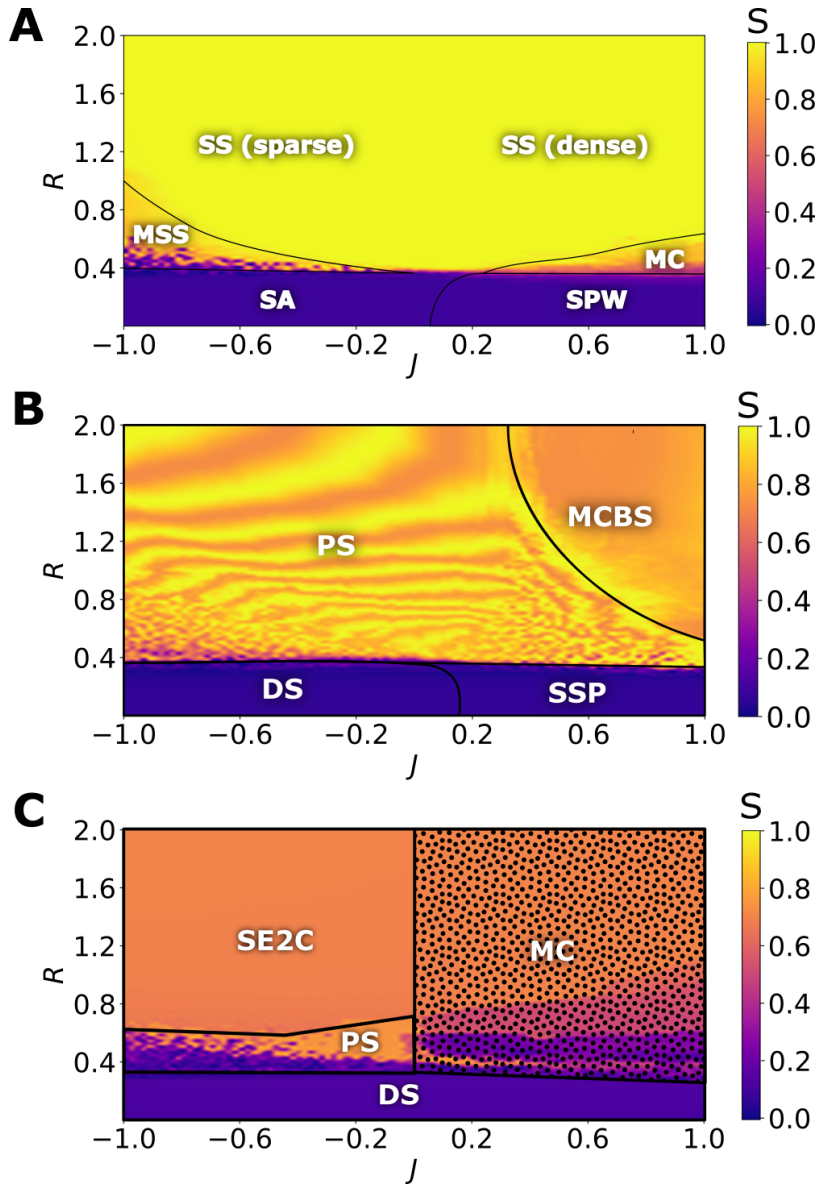


Fig. S17 Purely local attraction. Phase diagram in the (J, R) parameter space for $N = 100$ swarmalator collectives when $\varepsilon_r = 0$ and $\varepsilon_a = 0.5$. **(A)** In the absence of angular frequency $\omega = 0$. **(B)** Orthogonal angular frequencies $\omega_1 \perp \omega_2$. **(C)** Distributed orthogonal angular frequencies $\omega_1 \perp \omega_2$. The self-organizing emergent states observed in the depicted phase diagrams are static async (SA), static phase wave (SPW), mixed synchronized state (MSS), multi-cluster (MC), sparse and dense synchronized states (SS), disordered spin (DS), spinning spiky states (SSP), pumping state (PS), multi-cluster bouncing state (MCBS) and static embedded two-cluster (Static E2C).

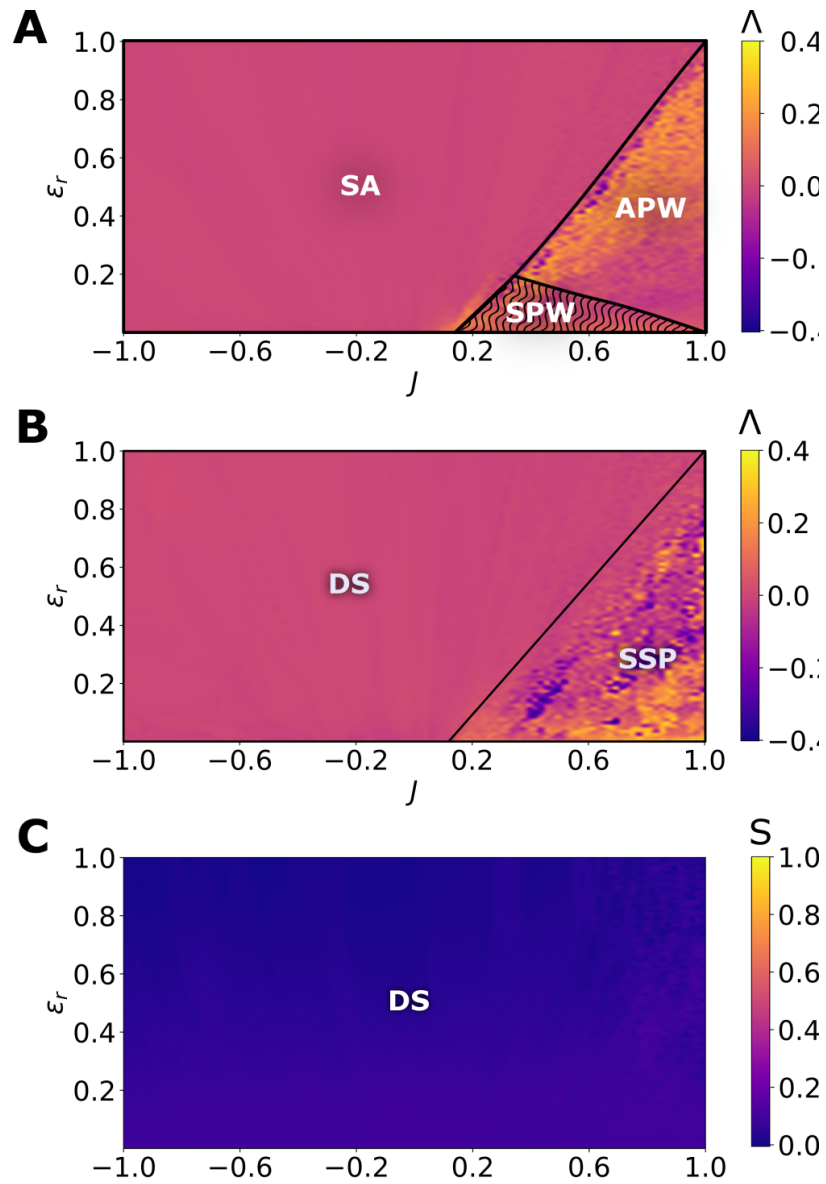


Fig. S18 Global repulsion interaction. Phase diagram in the (J, ε_r) parameter space for $N = 100$ swarmalator collectives and $R = 0.0$. (A) In the absence of angular frequency $\omega = 0$. (B) Orthogonal angular frequencies $\omega_1 \perp \omega_2$. (C) Distributed orthogonal angular frequencies $\omega_1 \perp \omega_2$. The self-organizing emergent states observed in the depicted phase diagrams are static async (SA), static phase wave (SPW), active phase wave (APW), disordered spin (DS), and spinning spiky states (SSP).

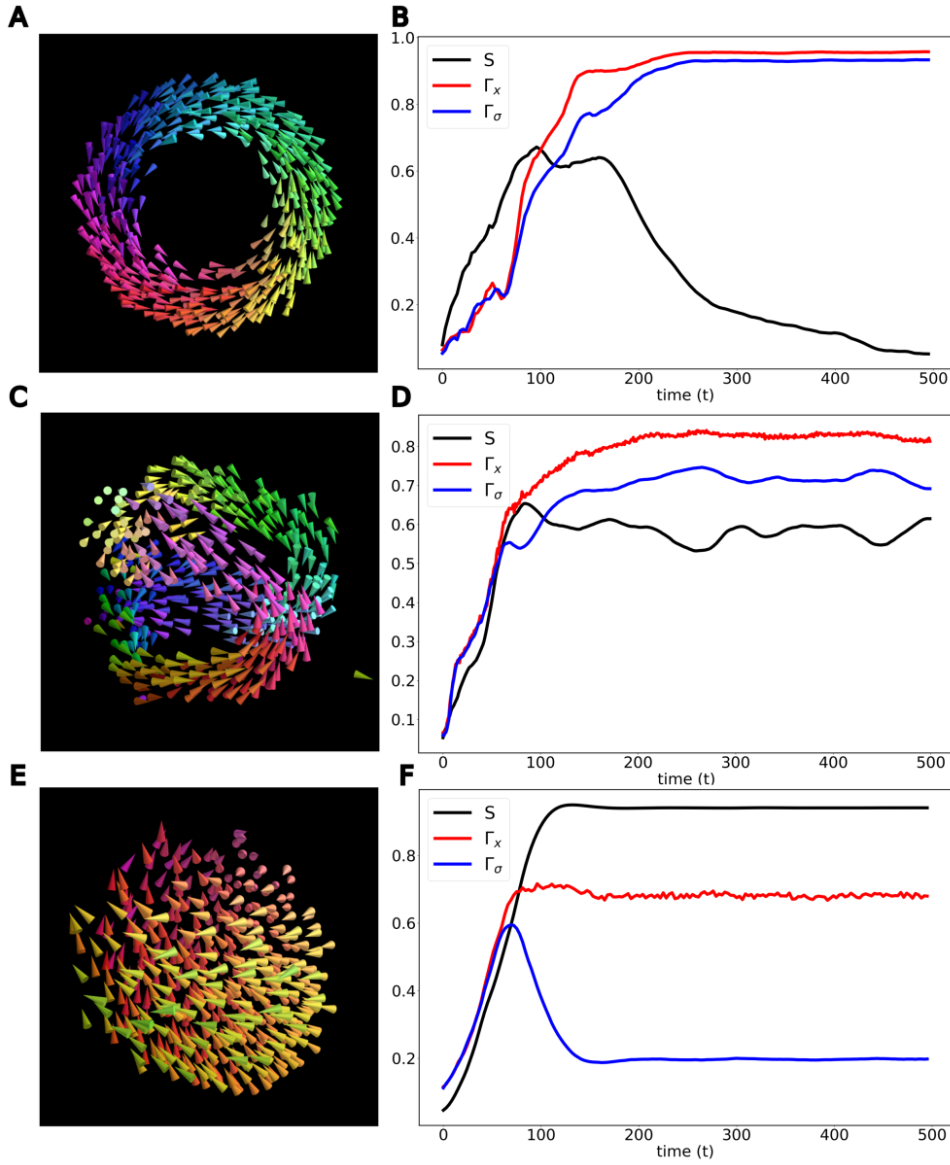


Fig. S19 Schooling of fish. Simulations are performed for $N = 500$ with the Gaussian noise with noise strength ($D_{x_k} = 0.005, D_{\sigma_k} = 0.005$). The corresponding plots on the right show the evolution of macroscopic parameters ($S, \Gamma_x, \Gamma_\sigma$) with time characterizing the collective behavior of the school. ($c = 0.5$, box size = 1.5, $\Delta = 0.8$, bound size = $\sqrt{3}/2 \cdot \text{box size} + \Delta$). (**A** and **B**) Milling behavior is observed for $R = 0.2, J = 0.5, \varepsilon_a = 0.9, \varepsilon_r = 0.0$. Simulations are performed for $N = 500$. (**C** and **D**) Stripes formation for $R = 0.2, J = 0.3, \varepsilon_a = 0.5, \varepsilon_r = 0.0$. (**E** and **F**) Rotating crystal for $N = 500, R = 1.0, J = 0.9, \varepsilon_a = 0.3, \varepsilon_r = 0.0$. Refer supplementary text S11 for discussions about the model and the order parameters.

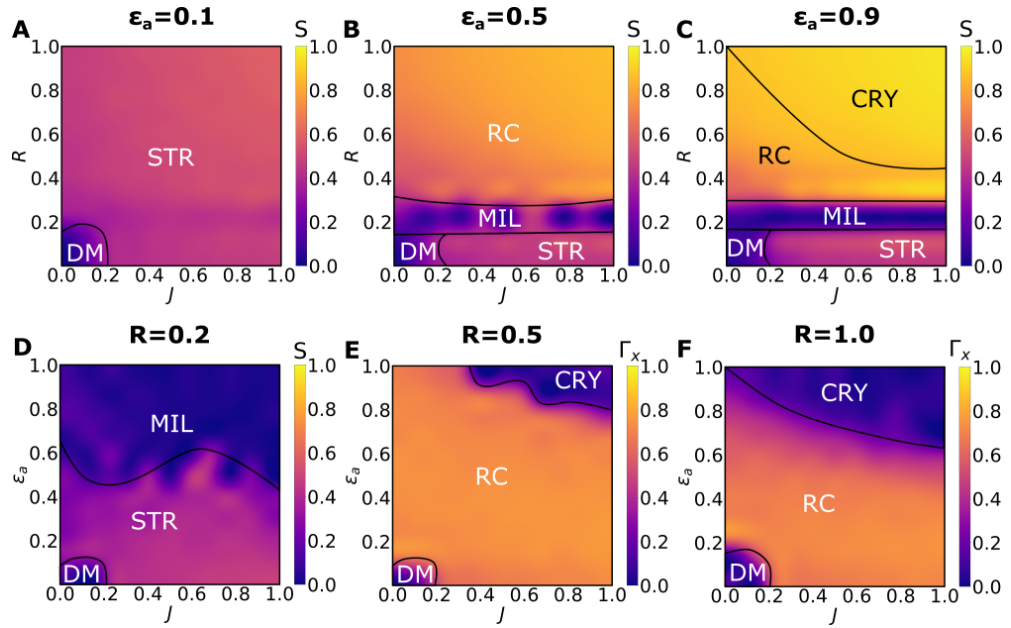


Fig. S20 Phase diagrams for school of fish. Two parameter phase diagrams of school of fish for $N = 100$ (A) in (J, R) parameter space and (B) in (J, ε_a) parameter space. The self-organizing emergent states observed in the depicted phase diagrams are stripes (STR), milling (MIL), rotating crystal (RC), and disorder motion (DM).

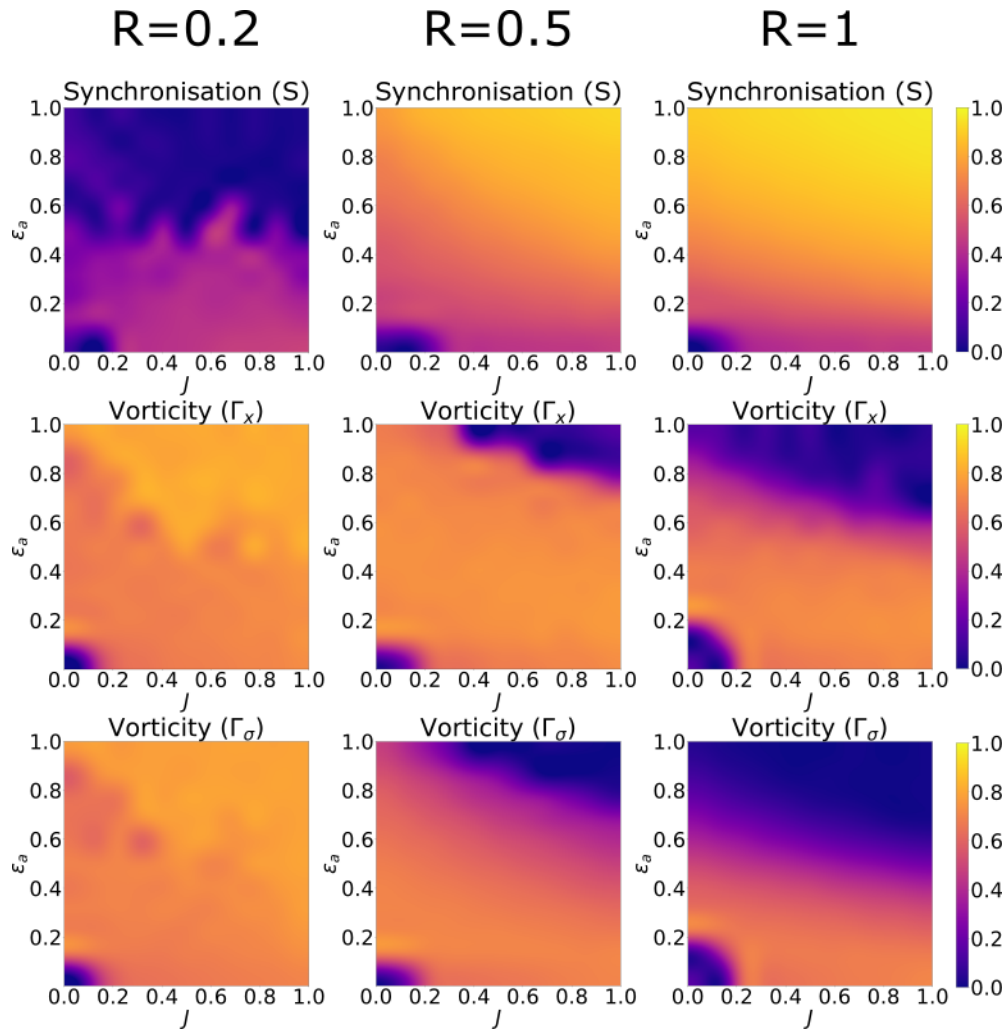

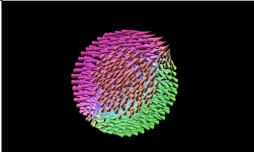
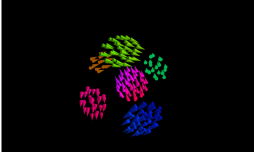
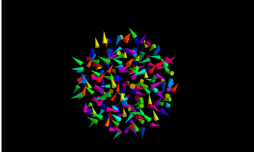

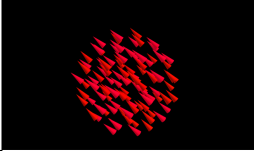
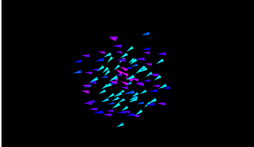
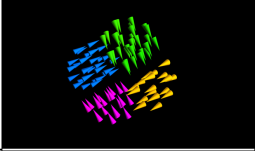
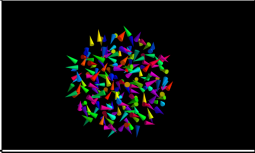

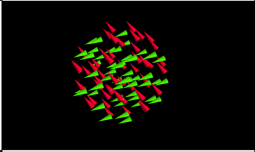
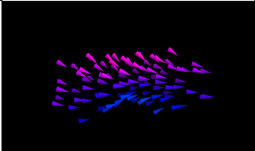
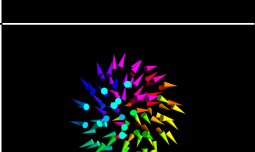
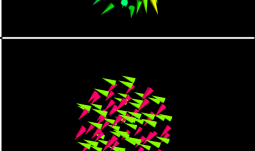
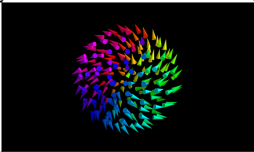
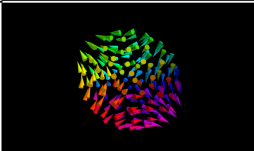
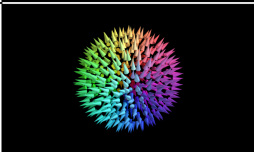
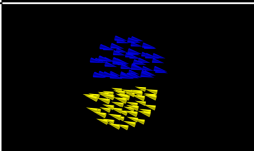
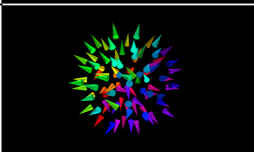
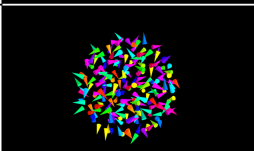
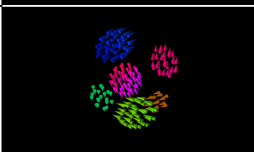


Fig. S21 Heat maps for school of fish. Heat maps of the synchronization order parameter (S), spatial vorticity parameter (Γ_x) and phase vorticity (Γ_σ) in (J, ϵ_a) parameter space.

SI no.	Snapshot	States	Type Interaction
1.		Static Sync (SS) <i>See movie S1</i>	Nonchiral ADCPI, RDCPI, EARCPI, LA
2.		Chimera (CH) <i>See movie S2</i>	Nonchiral ADCPI, RDCPI, EARCPI
3.		Multi-Cluster (MC) <i>See movie S3</i>	Nonchiral ADCPI, RDCPI, EARCPI, LA
4.		Static async (SA) <i>See movie S4</i>	Nonchiral ADCPI, RDCPI, EARCPI, LA, GR
5.		Active phase wave (APW) <i>See movie S5</i>	Nonchiral ADCPI RDCPI, EARCPI, GR
6.		Synchronised spinning state (SSS) <i>See movie S6</i>	Chiral ADCPI
7.		Pumping state (PS) <i>See movie S7</i>	Chiral ADCPI, LA

SI no.	Snapshot	States	Type Interaction
8.		Multi-cluster bouncing state (MCBS) <i>See movie S9</i>	Chiral LA, RDCPI, ADCPI, EARCPI
9.		Disordered spin (DS) <i>See movie S10</i>	Chiral ADCPI, EARCPI, RDCPI, PLA, GR
10.		Spinning spiky state (SSP) <i>See movie S11</i>	Chiral ADCPI, RDCPI, EARCPI, LA, GR
11.		Static embedded 2 clusters (SE2C) <i>See movie S12</i>	Chiral LA, ADCPI
12.		Turning tube (TT) <i>See movie S13</i>	Nonchiral EARCPI
13.		Active core spiky state (ACSP) <i>See movie S14</i>	Nonchiral RDCPI, EARCPI
14.		Breathing state (BS) <i>See movie S15</i>	Nonchiral RDCPI, EARCPI

SI no.	Snapshot	States	Type Interaction
15.		Static phase wave (flower) (SP) <i>See movie S16</i>	Nonchiral RDCPI, EARCPI, LA, GR
16.		Static phase wave (twisted) (SP) <i>See movie S17</i>	Nonchiral RDCPI, EARCPI, LA, GR
17.		Spiky state (star) (SP)	Nonchiral RDCPI, EARCPI, LA, GR
18.		Bouncing 2 clusters (B2C) <i>See movie S18</i>	Chiral EARCPI
19.		Active core spinning spiky state (ACSSP) <i>See movie S19</i>	Chiral RDCPI, EARCPI
20.		Active async (AA) <i>See movie S20</i>	Chiral RDCPI, EARCPI
21.		Spinning clusters (SC) <i>See movie S21</i>	Nonchiral RDCPI

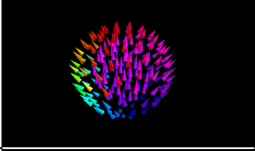
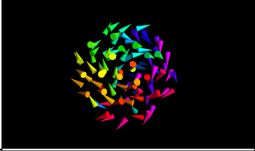
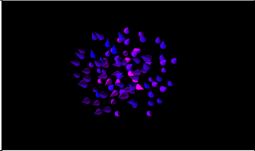
SI no.	Snapshot	States	Type Interaction
22.		Spinning chimera (SCH) <i>See movie S22</i>	Chiral RDCPI
23.		Repulsive mixed phase wave (RMPW) <i>See movie S23</i>	Nonchiral RDCPI
24.		Mixed static sync (MSS) <i>See movie S24</i>	Nonchiral LA

Table S1. Gallery of observed self-organizing collective states. A zoo of self-organizing collective states observed in the vast range of parameters are listed in the table. ‘Nonchiral’ corresponds to the interactions among the swarmalators in the absence of angular frequency for the orientation vectors, whereas ‘chiral’ corresponds to the interactions among the swarmalators with orthogonal angular frequencies. Furthermore, ‘ADCPI’ refers to ‘attractive dominated competitive phase interaction’, ‘RDCPI’ refers to ‘repulsion dominated competitive phase interaction’, ‘EARCPI’ refers to ‘equal repulsion and attraction competitive phase interaction’, ‘LA’ refers to ‘local attraction’, and ‘GR’ refers to ‘global repulsion’.

Movie S1.

Static sync. The movie shows the time evolution of static sync state (SS). Initially randomly distributed swarmalators synchronize their orientations and congregate into a single static cluster.

Movie S2.

Chimera state. The movie shows a complete and cross-sectional view of chimera state (CH) development during the transition from static async to static sync and back as a function of the vision radius R . The synchronized core emerges from the center of the static async state and turns into static sync state for higher values of R .

Movie S3.

Multi-Cluster state. The movie shows the time evolution of multi-cluster state (MC).

Movie S4.

Static async. The movie shows the time evolution of static async state (SA). Initially randomly distributed swarmalators desynchronize their orientations and congregate into a single static cluster.

Movie S5.

Active phase wave. The movie shows the time evolution of active phase wave (APW).

Movie S6.

Sync spinning state. The movie shows the time evolution of synchronized spinning state (SSS). Initially randomly distributed swarmalators synchronize their orientations and congregate into a single spinning (precessing) cluster. This precession effect happens in the presence of orthogonal angular frequencies applied to the population.

Movie S7.

Pumping State. The movie shows the time evolution of pumping state (PS) observed in the case of two orthogonal angular frequencies. This state involves period-2 oscillation of a single cluster.

Movie S8.

Oscillation Death. The movie shows the oscillation death in swarmalators with distributed frequencies.

Movie S9.

Multi-Cluster bouncing state. The movie shows the time evolution of the multi-cluster bouncing state (MCBS). The inter-cluster separation increases and decreases periodically.

Movie S10.

Disordered spin state. The movie shows the time evolution of disordered spin state (DS). The initially randomly distributed swarms desynchronize their orientations and congregate into single spinning (precessing) cluster. This precession effect can be attributed to the presence of angular frequencies.

Movie S11.

Spinning spiky state. The movie shows the time evolution of spinning spiky state (SSP). This precession effect can be attributed to the presence of two orthogonal angular frequencies.

Movie S12.

SE2C state. The movie shows the time evolution of static embedded two-cluster state (SE2C). The oscillation death in pumping state results in static embedded two-cluster.

Movie S13.

Turning tube state. The movie shows the time evolution of turning tube (TT) state. The elongation of static sync state in $J < 0$ region with finite vision radius results in two cylindrical formation that shows collective rotation.

Movie S14.

Active core spiky state. The movie shows the time evolution of active core spiky (ACSP) state. The turbulent core emerges from center of static spiky state and turns into active async state for higher values of R .

Movie S15.

Breathing state. The movie shows the time evolution of breathing state (BS). The dynamics consists of cyclic expansion and contraction of static embedded two cluster state.

Movie S16.

Flower state. The movie shows the time evolution of flower state (SP).

Movie S17.

Twisted state. The movie shows the time evolution of twisted state (SP).

Movie S18.

Bouncing two cluster. The movie shows the time evolution of bouncing two-cluster (B2C) state.

Movie S19.

Active core spinning spiky state. The movies shows the time evolution of active core spinning spiky (ACSSP) state. The turbulent core emerges from center of spinning spiky state and turns into an active async state for higher values of R .

Movie S20.

Active async. The movie shows the time evolution of active async state.

Movie S21.

Spinning cluster state. The movie shows the time evolution of spinning (rotating) cluster state.

Movie S22.

Spinning chimera state. The movie shows the time evolution of spinning chimera state (SCH). A synchronized spinning (precessing) core emerges from the center of the spinning spiky state and turns into synchronized spiky state.

Movie S23.

Repulsive Mixed Phase Wave. The movie shows the time evolution of repulsive mixed phase wave (RMPW). The intermediate vision radius in the case of repulsive dominated competitive interaction between the orientation vectors converts the spinning spiky states into turbulent state.

Movie S24.

Mixed static sync. The movie shows the time evolution of mixed static sync (MSS). The state consists of synchronized and partially synchronized population.

Movie S25.

Fish schooling. The movie depicts the polarized and milling states in the extended swarmalator model. In polarized (crystal) state the fish synchronize their orientation, while during milling fish move in circular fashion.

Movie S26.

Fish schooling experimental analysis. This movie shows the visualization of fish schooling experimental data and corresponding order parameters used for characterizing the schooling dynamics.

Movie S27.

Traveling waves of genetic expression. This movie depicts the traveling phase wave in swarmalators in the presence of local spatial interactions, which resembles the traveling wave of gene expression in mouse embryo during embryonic development of vertebra segments.

Movie S28.

Cell sorting. This movie depicts the swarmalator analog of the cell sorting process for two and three types of cells. Random distribution of swarmalators spontaneously sort themselves into layers due to differential spatial coupling.

Movie S29.

Aggregation in slime mold. This movie depicts the aggregation of swarmalators in the presence of local spatial interactions. The emerging structure resembles the cellular aggregation of slime mold to form a multi-cellular organism.

References

- [1] Humaira, H., Rasyidah, R.: Determining the appropriate cluster number using elbow method for k-means algorithm (2020) <https://doi.org/10.4108/EAI.24-1-2018.2292388>
- [2] Hartigan, J.A., Wong, M.A.: Algorithm as 136: A k-means clustering algorithm. *Applied Statistics* **28**, 100 (1979) <https://doi.org/10.2307/2346830>
- [3] Kanungo, T., Mount, D.M., Netanyahu, N.S., Piatko, C.D., Silverman, R., Wu, A.Y.: An efficient k-means clustering algorithms: Analysis and implementation. *IEEE Transactions on Pattern Analysis and Machine Intelligence* **24**, 881–892 (2002) <https://doi.org/10.1109/TPAMI.2002.1017616>
- [4] Tunstrøm, K., Katz, Y., Ioannou, C.C., Huepe, C., Lutz, M.J., Couzin, I.D.: Collective states, multistability and transitional behavior in schooling fish. *PLOS Computational Biology* **9**(2), 1–11 (2013) <https://doi.org/10.1371/journal.pcbi.1002915>
- [5] Berdahl, A., Torney, C.J., Ioannou, C.C., Faria, J.J., Couzin, I.D.: Emergent sensing of complex environments by mobile animal groups. *Science* **339**(6119), 574–576 (2013) <https://doi.org/10.1126/science.1225883>
<https://www.science.org/doi/pdf/10.1126/science.1225883>
- [6] Ioannou, C.C., Guttal, V., Couzin, I.D.: Predatory fish select for coordinated collective motion in virtual prey. *Science* **337**(6099), 1212–1215 (2012) <https://doi.org/10.1126/science.1218919>
<https://www.science.org/doi/pdf/10.1126/science.1218919>
- [7] Hamilton, W.D.: Geometry for the selfish herd. *Journal of Theoretical Biology* **31**(2), 295–311 (1971) [https://doi.org/10.1016/0022-5193\(71\)90189-5](https://doi.org/10.1016/0022-5193(71)90189-5)